UTRECHT UNIVERSITY
Institute for Marine and Atmospheric Research Utrecht

Universiteit Utrecht

Seasonality of Atmospheric CH_4 and $\delta^{13}CH_4$

New measurement at IMAU and analysis of Global long-term time series and model data

Xietiancheng Yu
5108284

Supervisors:

Prof. dr. Thomas Röckmann
Dr. Bibhasvata Dasgupta
Dr. Rupert Holzinger

July 11, 2024

Contents

Abstract

In this project, we measured methane samples at the Institute for Marine and Atmospheric Research Utrecht (IMAU) and analyzed long-term time series observations from NOAA as well as model outputs to explore the seasonality of CH_4 and $\delta^{13}CH_4$.

In the first part, we measured surface flask samples from two IMAU methane stable isotope measurement projects and compared them with NOAA/INSTAAR measurements. The results show that after quality control, data cleaning and offset correction, our $\delta^{13}CH_4$ measurements agree well with the INSTAAR results and show consistent seasonality.

In the second part, we analysed the NOAA long-term time series of CH_4 and $\delta^{13}CH_4$ at 18 stations. In the southern hemisphere,there is a negative correlation between the seasonality of CH_4 and $\delta^{13}CH_4$, their seasonality is mainly controlled by OH sink. In the Northern Hemisphere, the anti-correlation is not significant, the seasonality of $\delta^{13}CH_4$ is more affected by emissions rather than OH sink.

Using the Miller & Tans method, we use smooth fit and trend as two different backgrounds and obtain the corresponding source $\delta^{13}CH_4$. We find that the regional source $\delta^{13}CH_4$ in the Northern Hemisphere has a clear seasonality, which is mainly controlled by regional emissions, and has seasonal characteristics consistent with microbial emissions.

CH_4 and $\delta^{13}CH_4$'s seasonal amplitudes and source $\delta^{13}CH_4$ show latitudinal gradients, which are related to the distribution of emission and $\delta^{13}CH_4$. High latitudes show stronger seasonality and more depleted isotopic signals, indicating that they are more related to microbial emissions. In contrast, the proportion of enriched emissions is higher in mid- and low-latitude regions.

The high-latitude CH_4 seasonal amplitudes show downward long-term trends, accompanied by a depletion trend of regional source $\delta^{13}CH_4$, indicating an increase in the proportion of wetland emissions. The inter-annual trend in mid- and low-latitudes is less obvious, which may be masked by fossil or pyrogenic emissions.

The inverse model can reproduce the long-term trend and seasonal cycle of CH_4 well but underestimates the seasonality of $\delta^{13}CH_4$. The discrepancy of seasonality of source $\delta^{13}CH_4$ between the inverse model and observations highlights the potential underestimation of high-latitude microbial emissions and mid- and low-latitude fossil fuel emissions. More $\delta^{13}CH_4$, $\delta D - CH_4$ observations in emission regions are required, especially in tropical regions, to better constrain emission sources and sinks.

1 Introduction

1.1 Research background

Methane is the second most important greenhouse gas in the atmosphere, which has approximate 30 times global warming potential over a 100-year horizon (GWP-100) than CO_2 Forster et al. [2021]. In recent years, atmospheric methane concentration has been rising rapidly and accelerating.

Accroding to Canadell et al. [2021], there are three main sources of methane in the atmosphere: microbial sources, fossil sources, and pyrogenic sources. Microbial sources include natural sources, mainly wetland emissions, and anthropogenic sources, mainly agriculture and waste. Fossil sources come mainly from the use of fossil fuels. Pyrogenic sources come mainly from the biomass combustion process.

The lifetime of atmospheric methane is about 9 to 10 years, among which the oxidation of tropospheric OH is its most important removal process(EHHALT [1974], Basu et al. [2022], Nisbet et al. [2023]). At the same time, reactive chlorine in the atmosphere, stratospheric oxidation, and soil uptake also play a certain role in the removal of atmospheric methane.

Stable isotope analysis of methane refers to the analysis of the ^{13}C and ^{2}H in methane. Due to the difference in molecular mass caused by the different isotope compositions of methane, it will further isotopic fractionation, showing different isotope signatures. The isotope composition is usually reported by δ notation (see section 1.2)

Different sources often have different methane isotope signatures, the global average $\delta^{13}CH_4$ for all sources is approximately -54‰(Sherwood et al. [2017], Nisbet et al. [2023]), among which the isotope signatures of microbial sources are more depleted, while the isotope signals of fossil sources and pyrogenic sources are more enriched, as shown in Fig. 1. At the same time, emissions from different sources also contain different seasonal characteristics, which will influence both the methane concentration and δ value (Kangasaho et al. [2022]). Therefore, by analyzing the time series of methane and its δ value, it is possible to get more information on the source of methane in the atmosphere.

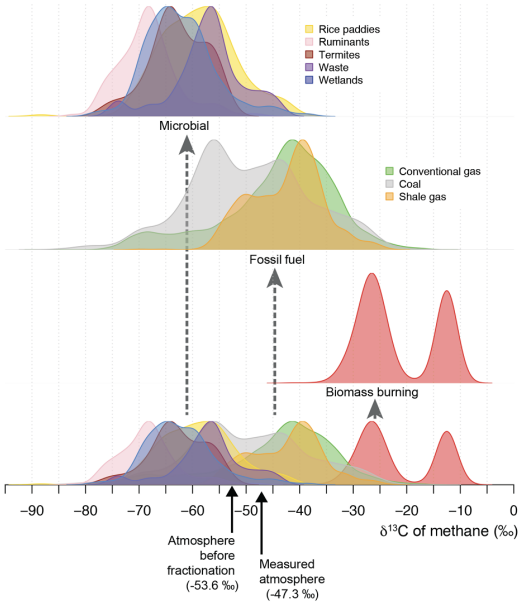

Figure 1: Normalized probability density distributions for the $\delta^{13}CH_4$ of microbial, fossil, and biomass burning sources of methane (Sherwood et al. [2017])

In recent years, many studies have been conducted that analyze time series of CH_4 through long-term observations to study the rapidly increasing levels of methane in recent years. The seasonal cycle of

methane is also analyzed. The seasonality of methane is mainly caused by emissions or sinks with seasnoal characteristics, such as microbial emission, pyrogenic emission, and OH sink, which may provide us with the reason for the rapidly increasing methane level in recent years.

In previous research, the seasonal cycle of methane was studied at high latitudes in the Northern Hemisphere. Intuitively, increasing methane levels in the atmosphere would be expected to increase the amplitude of seasonal cycle, but they found through surface flask observations and model simulations that the results at high northern latitudes are contrary to expectations, which mainly due to increasing boreal wetland emissions (Barlow et al. [2016]). The emission from the Middle East and East Asia could also contribute to the change of CH_4 seasonal cycle amplitude at NH high latitude (Dowd et al. [2023]).

However, few studies have yet focused on the seasonal cycle of methane isotopes. Since the isotope signature is closely related to the emission and removal process of methane in the atmosphere, it is expected that its seasonality will also show some characteristics or inter-annual trends. The limitation of the study of seasonal cycles lies mainly in acquiring long-term observational data, especially for methane stable isotope composition. Among them, NOAA has a relatively complete $\delta^{13}CH_4$ time series, which can be used to analyze the seasonality of methane at different latitudes. However, in comparison to methane concentration data, the number of stations is fewer and the duration of the measurement is shorter.

Another problem in the analysis of the global methane isotope composition is how to compare data from various laboratories. Since the δ value to report the methane isotope composition is a relative value, each laboratory calibrates it to international standards. However, due to the laboratory environment, working standard material, and differences in measurement settings or instruments, there will still be some offsets between different laboratories, which was reported and determined in Umezawa et al. [2018].

In this study, we first started with our own measurements at the Institute for Marine and Atmospheric Research Utrecht (IMAU) stable isotope laboratory, by collaborating with other research institutions, we started to build quality control and offset correction rules between different labs. We compare our $\delta^{13}CH_4$ measurements with the NOAA long-term series and show the latest result of $\delta D - CH_4$ time series. In the second part, we analyzed the characteristics of methane isotopes at different latitudes based on NOAA global methane and its stable isotope time series and investigated its characteristics and variation of seasonality. By Miller&Tans method, we also combine both CH_4 and $\delta^{13}CH_4$ time series to get information on the source $\delta^{13}CH_4$ and its mean seasonal cycle. In the end, the data of the inverse model based on TM5 is also analysed and compared with observation, together with the information of emissions of three specific sources.

1.2 Methane isotope notation

In isotope analysis, due to the low abundance of heavier isotopes in nature, we often use δ value to represent the relative difference between the isotope ratio of a sample and the isotope ratio of a standard. This is usually expressed in the δ notation.

$$\delta = \left(\frac{\mathrm{R_{sample}}}{\mathrm{R_{standard}}} - 1 \right) \times 1000‰$$

where $\mathrm{R_{sample}}$ is the ratio of the heavy isotope to the light isotope in the sample, and $\mathrm{R_{standard}}$ is the ratio of the heavy isotope to the light isotope in the standard. For our CH_4 isotope measurement, since it is converted to CO_2 and H_2 first, the standard scales for $\mathrm{CH_4}$ isotope composition are international standard VSMOW (Vienna Standard Mean Ocean Water) and VPDB (Vienna Pee Dee Belemnite), which are used for D and ^{13}C respectively.

1.3 Overview on global methane and isotope time series

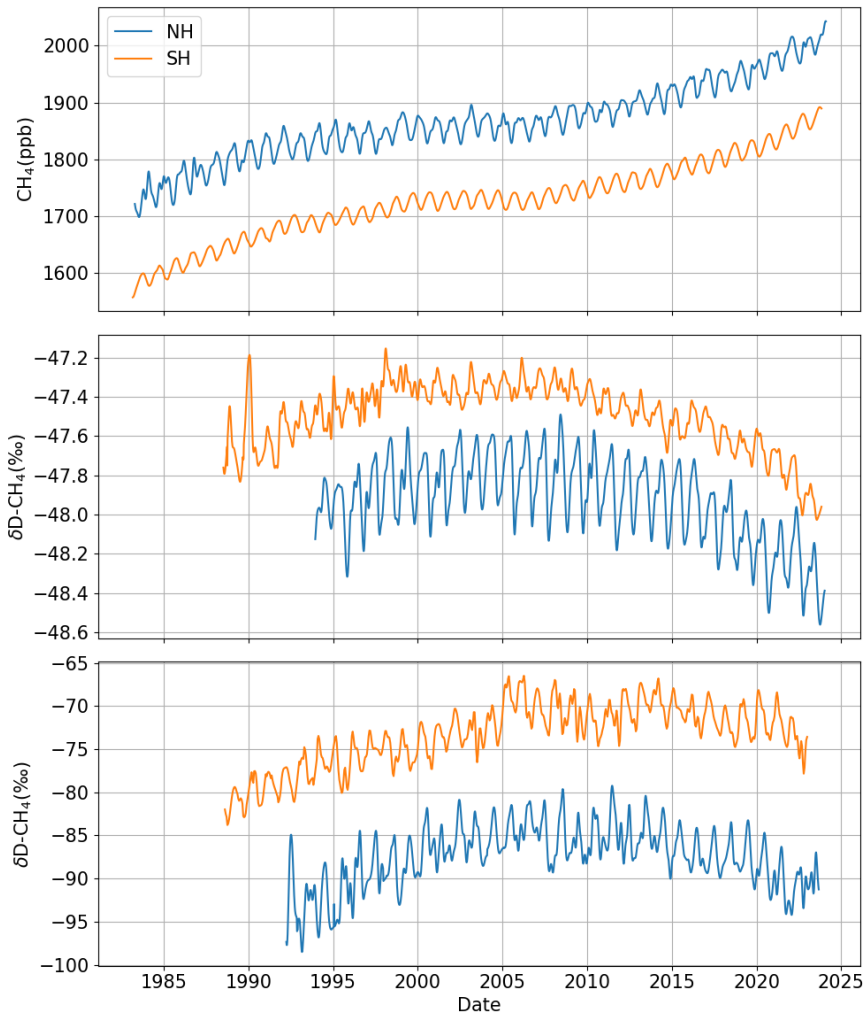

Figure 2: Overview of global methane time series

Over the past 40 years, methane growth has undergone three distinct phases, as shown in Fig. 2. From 1985 to 2000, the rate of methane increase gradually slowed down, accompanied by an enrichment of methane isotopes. Between 2000 and 2010, both methane concentration and δ values reached a stable phase. However, after 2010, methane began to rise again, showing a significant acceleration trend. Concurrently, the isotope trend reversed, shifting from enrichment to depletion.

For seasonality, the amplitude of these three values in the Northern Hemisphere is significantly greater than in the Southern Hemisphere. This disparity is likely due to the lower emissions in SH compared to the NH, especially in the high latitudes of SH, where seasonal variations are primarily driven by the atmospheric OH sink.

In conclusion, on a global scale, the rapid increase in methane in recent years is characterized by distinct isotopic features, indicating a significant change in the global methane budget structure, the microbial emission with depleted δ value resulted in the recent methane increase(Lan et al. [2021], Basu et al. [2022], Nisbet et al. [2023]).

2 Data and methods

2.1 IMAU methane project overview

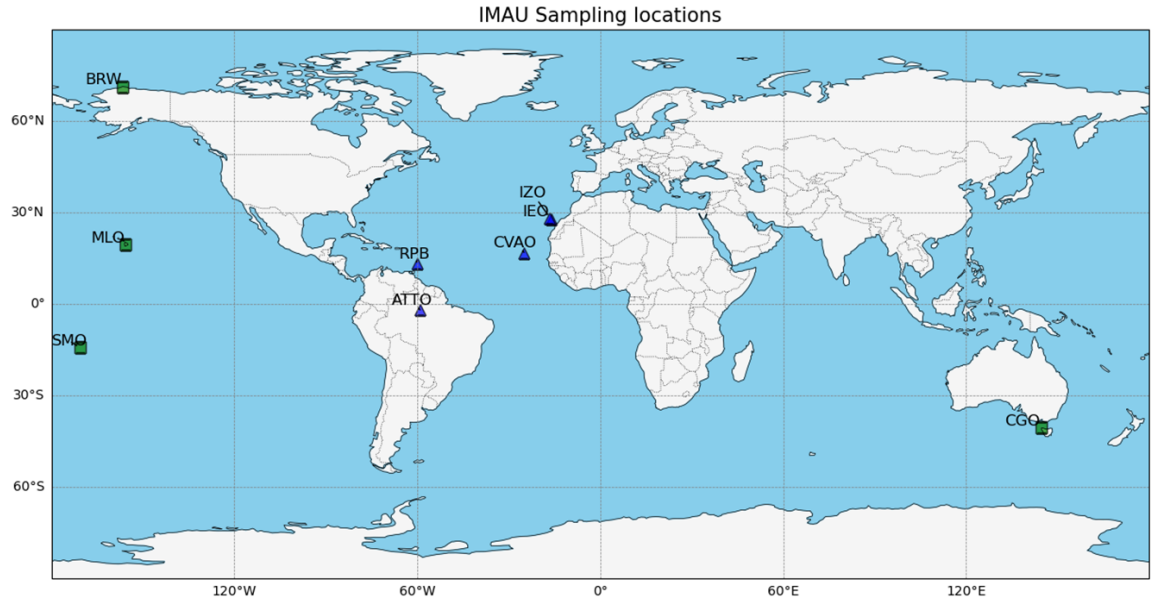

Figure 3: IMAU methane isotope measurement sites

Fig. 3 shows ongoing global methane stable isotope measurement projects currently being conducted by the IMAU Stable Isotope Lab. Four green squares represent the BUDS project, and five blue triangles represent the ISAMO project.

The BUDS (Boulder Utrecht Deuterium System) project is a collaborative project with INSTAAR (Institute of Arctic and Alpine Research). In this project, the remaining gas in methane sample flasks measured by NOAA GML (Global Monitoring Laboratory) is transferred to flexfoil bags using a sample transfer technique developed by INSTAAR and then shipped and remeasured at IMAU. The $\delta^{13}CH_4$ measurements are conducted at both labs for inter-laboratory quality control and to determine offsets, while $\delta D - CH_4$ measurements are conducted at IMAU to help INSTAAR rebuild its $\delta D - CH_4$ analysis system.

The ISAMO (Iron Salt Atmospheric Methane Oxidation) project aims to explore the oxidative removal of methane by reactive chlorine in the atmosphere. Methane flasks from the North Atlantic are regularly collected and subjected to isotope analysis at the IMAU lab. By studying the isotope data, the project seeks to understand the mechanisms by which atmospheric reactive chlorine removes methane. Here, we use flask samples from five fixed stations for comparison. Additionally, the ISAMO project also includes methane samples collected from ships sailing across the North Atlantic, which are not analyzed in this research.

2.2 IMAU methane stable isotope data measurement and calibration

2.2.1 Methane stable isotope measuring system at IMAU

The instrument we used to measure the methane isotopes at IMAU Stable Isotope Laboratory is a continuous-flow Isotope Ratio Mass Spectrometry (IRMS), which is described in Brass and Röckmann [2010].

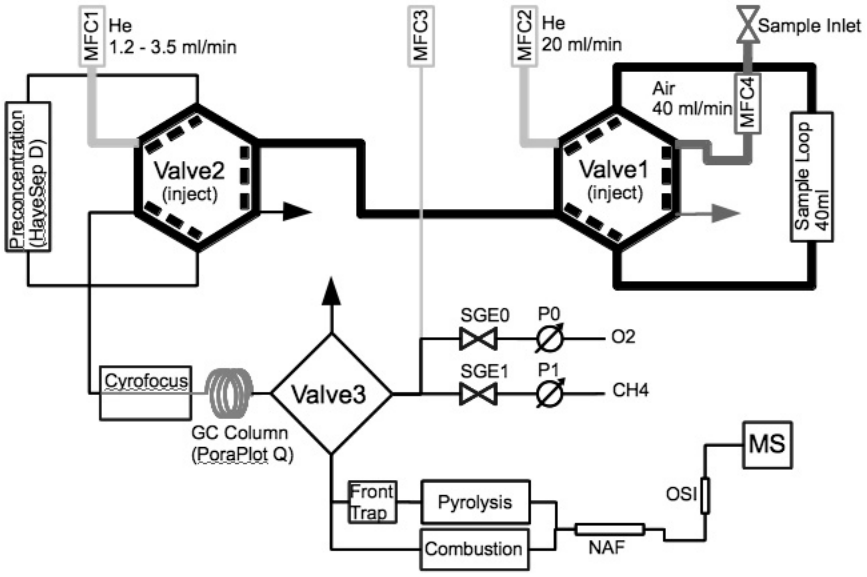

Figure 4: Scheme of methane analysis system from Brass and Röckmann [2010]

The system is divided into two similar parts, for $\delta^{13}CH_4$ and $\delta D - CH_4$ measurement respectively. The inlet part contains eight ports for samples and one for reference gas. For each sample flask, the sample is first injected into the δD analysis line, then injected into the $\delta^{13}C$ analysis line.

The analysis is included several processes, for both δD and $\delta^{13}C$:

First, the sample is connected to the port, before opening the valve of the sample flask, the inlet line is flushed to remove the possible pollution by remaining gas from previous samples, and then open the valve of the flask to fill the inlet line. This step is performed manually when we connect new samples.

Second, the sample is injected into the system, controlled by a Mass Flow Controller(MFC) to get a certain volume, in our measurement, the volume for δD and $\delta^{13}C$ measurements are set as 60 ml and 40 ml respectively.

Third, the gas is transported by N_2 to the pre-concentration unit, the column is first cooled down to -130℃, to trap the CH_4 on it and let the N_2, O_2 pass. Then the CH_4 is released by heating the column to -85℃, while the CO_2 and H_2O remain on the column. The remaining gas is removed by heating the column to 70℃ after CH_4 is transferred to the next unit.

Fourth, since the volume of the CH_4 from the pre-concentration step is still large, it will make the peak in the Mass Spectrometry too wide to analyse. Hence, in the cryofocus unit, the methane is focused into a smaller volume by the GC column at -150 to -135℃, and then released at 50℃.

It is quite difficult to measure the isotope composition of CH_4 directly, so to measure the $\delta^{13}C$ and δD value, we first have to convert the CH_4 to CO_2+H_2O and H_2+C, by Combustion and Pyrolysis oven respectively. For $\delta^{13}C$, the combustion is performed at an Alumina tube at 1130℃, and there is a dryer (NAF) after that to remove water vapour. For δD, the pyrolysis is performed in a Silica tube at around 1330℃.

Then the H_2 or CO_2 is introduced into the MS by Open Split Interface (OSI) for δD or $\delta^{13}C$ isotope analysis.

For our CH_4 isotope measurement, the standard scale for CH_4 isotope composition are VSMOW (Vienna Standard Mean Ocean Water) and VPDB (Vienna Pee Dee Belemnite), which are used for δD and $\delta^{13}C$ respectively.

2.2.2 Methane isotope calibration

In our measuring system, all measurement results are expressed as δ values based on VPDB and VSMOW standards. However, due to potential isotopic fractionation by the instrument during the measurement process, it is necessary to introduce a reference gas cylinder with known mixing ratio and δ values, also known as a working gas. By measuring the working gas between sample measurements, the measurement results of the working gas and its known standard value can be used to calibrate the sample results from the measuring system, thereby eliminating the influence of the isotopic fractionation effect generated by the instrument during the measurement process and ensuring the accuracy of the isotopic measurements of the samples.

In our methane stable isotope measurement, a reference gas cylinder with 1985.24 ppb CH_4 and $\delta^{13}CH_4$= -48.09‰ and $\delta^{13}CH_4$= -90.91‰ as fixed value is used. For every 4 measurements of sample flasks, the reference gas is measured three times both before and after.

Reference value determination Since the reference gas is measured before and after the sample, we first need to infer the reference value at the time of sample measurement, by following steps:

First, extracting the reference gas measurement data. As shown in Fig. 9, the system is not always stable. To remove the outliers, a simple filter is applied in this step,. As shown in table 1

Table 1: Filter of outliers for reference gas

Species	Area	Width	δ	Peak Start (s)	Peak End (s)
^{13}C	[2, 13]	[25, 70]	[-70, -20]	270	340
D	[2, 13]	[20, 70]	[-270, -50]	200	250

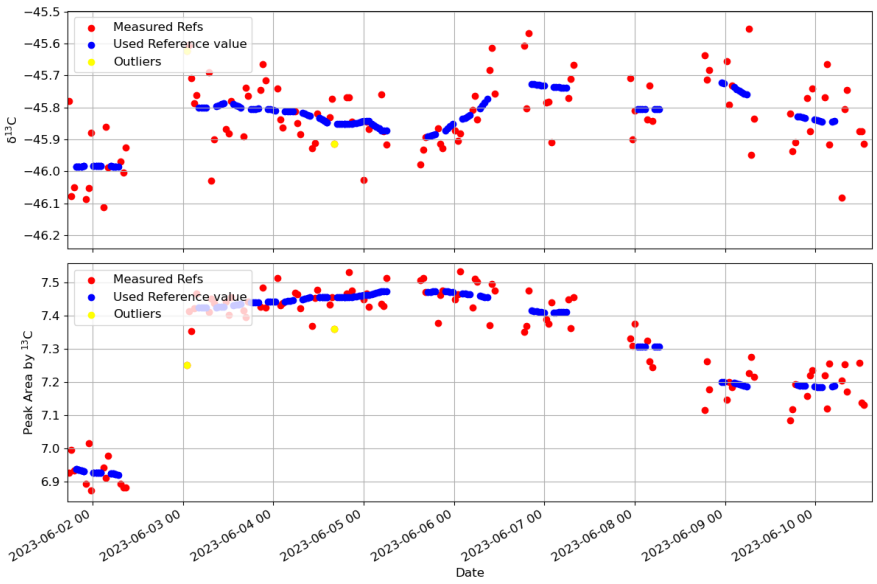

Figure 5: Reference value determination($\delta^{13}C$ and peak area for example)

After removing the obvious outliers, some minor outliers remain, as indicated by the yellow dots in the figure. These may occur randomly due to unstable voltage. However, the values of the reference gas should remain overall stable over short periods, as the gas cylinder has a fixed standard value. To remove this influence, A 24-hour window was selected centred on each data point, within each window, the robust Z-score for the centre point is calculated based on the MAD (Median Absolute Deviation). We chose this indicator rather than the standard Deviation because our reference gas data does not conform to a Gaussian distribution and outliers in our data will have significant impact on the mean

value and standard deviation. While the MAD and median is less influenced by the outliers in the data.

The robust Z-Score is given by:

$$\text{MAD}(X) = 1.4826 \times \text{Median}(|X - \text{Median}(X)|) \tag{2.1}$$

$$\text{Robust Z-Score} = \frac{x_i - \text{Median}(X)}{\text{MAD}(X)} \tag{2.2}$$

where 1.4826 is the usual factor to match the MAD with the scale of standard deviation (σ) at Gaussian distributions(Rousseeuw and Croux [1993]).

For each reference gas measurement, if the absolute value of robust Z-score for one of the isotope value or peak area is higher than 3, this point will be removed.

After all outliers are removed, a 24-hour rolling average can be performed on our cleaned reference data to get a relatively stable reference line, and by KNeighborsRegressor using 6 neighbour value and distance weight to interpolate, the reference value at sample measurement time can be inferred, which is shown as the blue points in Fig. 5.

Sample result calibration Then, using the measured working gas value, the working gas cylinder standard value and the sample measurement value, the sample calibrated δ value and mixing ratio can be calculated by eq. (2.3) and eq. (2.4).

$$\delta_{sample-calibrated} = \left(\frac{(\delta_{sample-working} + 1) \times (\delta_{ref-standard} + 1)}{\delta_{ref-working} + 1} - 1\right) \times 1000‰ \tag{2.3}$$

$$\text{Mixing ratio}_{\text{sample}} = \frac{\text{Peak Area}_{\text{sample}}}{\text{Peak Area}_{\text{Ref-working}}} \times \text{Mixing ratio}_{\text{Ref-standard}} \tag{2.4}$$

where the 'working' subscript means the reference value we measured between sample measurement, and 'standard' means the fixed value of the reference gas cylinder.

2.3 Sample Data quality control

After calibrating our measurement data, we still need to perform some quality control steps on the sample data to avoid potential problems with the sample flasks during the sampling or transportation process that could lead to inaccurate results.

For the BUDS data, since the samples were already analyzed for δ^{13}C at the INSTAAR laboratory before being shipped to IMAU for analysis, we can compare the δ^{13}C data and methane mixing ratios measured at INSTAAR and IMAU to conduct preliminary quality control.

Here, we primarily use two indicators, the δ^{13}C difference and the Methane concentration growth rate, which are represented as follows:

$$\text{Growth Rate} = \frac{\text{Mixing ratio}_{\text{IMAU}} - \text{Mixing ratio}_{\text{INSTAAR}}}{\text{Mixing ratio}_{\text{INSTAAR}}} \tag{2.5}$$

$$\delta^{13}\text{C diff} = \delta^{13}\text{C}_{\text{IMAU}} - \delta^{13}\text{C}_{\text{INSTAAR}} + 0.15 \tag{2.6}$$

where 0.15 is the δ^{13}C offset between IMAU and INSTAAR (seesection 2.4)

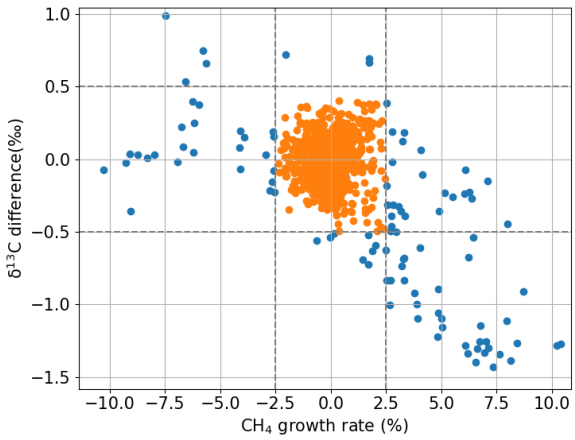

Figure 6: Quality control between INSTAAR and IMAU

If the absolute value of the δ^{13}C difference exceeds 0.5‰, or if the methane mixing ratio growth rate is higher than 2.5%, as indicated by the blue dots in the figure, we will mark the sample flask as unstable and disregard its data in subsequent analyses. These samples may have been leaked or polluted during transportation.

Next, we group the data by different stations and sort it by sampling time to obtain time series for each station. Clearly, within these time series, we will also find some outliers. For analyzing the seasonality of the time series, these outliers often represent random emissions or pollution during the sampling process that need to be removed.

We apply a similar method on the time series data of the samples as described in section 2.2.2. However, due to the low and irregular frequency of our flask sampling, compared to the 24 hours used by the reference gas, here we use an 80-day window. At the same time, due to the many uncertainties in the sampling process, compared to continuous and repeated reference gas measurements, we need to be cautious in removing the data here. Taking these reasons into consideration, we performed two cleanups here. We used the points obtained from the first cleanup for a second calculation to obtain new rolling median values and MAD. Then, we judged all the original data by the range of the new rolling median $\pm$ 3MAD to determine the points that need to be removed. Through this modification, for sparse time series, the large error range caused by outliers can be reduced as much as possible, to prevent some outliers are not removed, and some points can be prevented from being deleted incorrectly in the first clean.

Fig. 7 shows an example of our data cleaning process, where the shaded areas represent the range of the median plus or minus three times the median absolute deviation calculated within a 80-day moving window. Values outside this range are marked as outliers and excluded. Please note that some points in the range are also removed because they are outside the range in other data (mixing ratio or delta). We applied the same method to our IMAU data from various stations and methane isotopes.

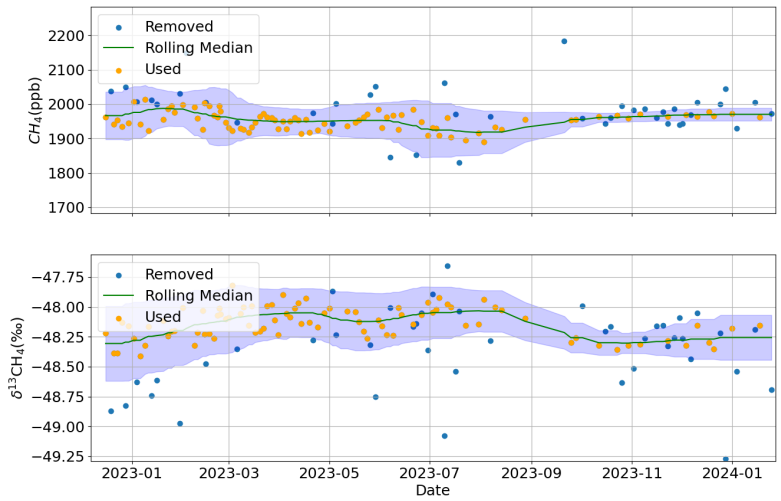

Figure 7: Example of data cleaning, CH_4 and $\delta^{13}CH_4$ from IZO

2.4 Offsets between different laboratories

Since the δ value is used for the measurement of methane isotopes, in order to better compare the spatial and temporal distribution of global methane data, it is necessary to calibrate the measurements of each laboratory to a unified standard. Although each laboratory uses the two international standards VPDB and VSMOW as the final standard for reporting δ values, in order to calibrate the measured values to this standard, each laboratory still needs to use reference materials with known δ values under the international scale for laboratory calibration to eliminate the isotope fractionation effect existing in the measurement system. Therefore, for different laboratories, the differences in their instruments or the selection of reference materials will still cause a certain offset to the delta values measured by each laboratory. Umezawa et al. [2018] reported the offset between 16 laboratories and also evaluated the specific offset values. Therefore, in order to better compare the methane isotope measurement data of IMAU and ISTAAR/NOAA, we uniformly moved the measurement values of the two laboratories to the MPI-BGC (Max Planck Institute for Biogeochemistry) standard. The specific offsets are shown in the table:

Table 2: Offset between IMAU and INSTAAR/NOAA

Institute	δ^{13}C	δD
MPI-BGC	0	0
IMAU	0.2	1.87
INSTAAR/NOAA	0.35	-11.04

2.5 NOAA long-term CH_4 and $\delta^{13}CH_4$ timeseries

Since the IMAU measurement project started recently, the amount of data currently is still not enough to explore the complete seasonal cycle and further seasonality changes between different years. Therefore, in addition to the sample data measured at IMAU, in this project, NOAA long-term time series are also used.

Methane concentration data and Stable Isotopic Composition of Atmospheric Methane come from the NOAA Global Monitoring Laboratory Carbon Cycle Cooperative Global Air Sampling Network.

For the methane concentration, the air samples are collected about every week and analysed at NOAA

GML in Boulder by gas chromatography with flame ionization detection or by cavity ring-down spectroscopy(Lan et al. [2023]).

For the $\delta^{13}CH_4$ data, the air samples from NOAA GML are analysed at the Stable Isotope Laboratory at the Institute of Arctic and Alpine Research (INSTAAR) by using either a Micromass Optima or Elementar Isoprime isotope-ratio mass spectrometer coupled to a methane a custom-built trapping system, a gas chromatograph, and a combustion furnace (Michel et al. [2023]).

The $\delta D - CH_4$ data was also analysed at INSTAAR from 2005 to 2009, however, the collection of data stopped since 2009 because of instrument and extraction manifold problems(White et al. [2016]).

NOAA uses different flags for the quality control of measurement data. In this study, for methane concentration, we used unflagged data. But in particular, for $\delta^{13}CH_4$ data, according to the provider, the data from 2018 to 2020 have been calibrated for amount effect, and the calibration method was introduced. To ensure the continuity of the data and better explore the seasonality, we retain these labelled data, that is, flagged as ..r and ..R. But the resulting seasonal cycles of these two years may not be true.

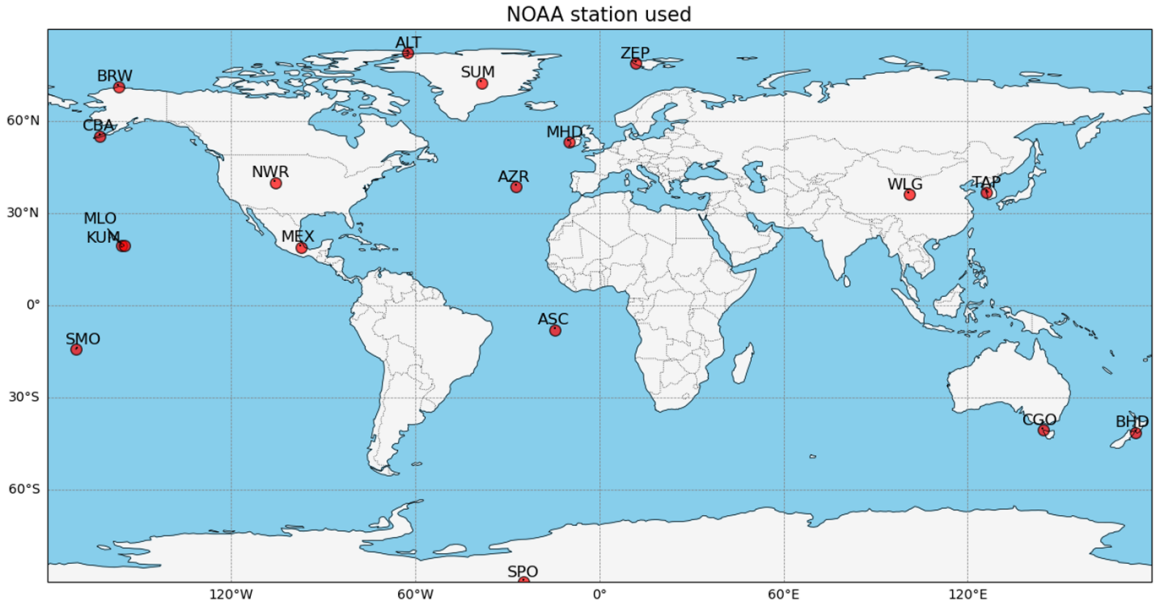

Figure 8: 18 NOAA stations used for analysis

For data selection, from all NOAA measurement stations, we chose those with complete isotope measurement data, as isotope measurements started later and at only limited stations compared to methane concentration measurements. Our selection criteria focused on stations that cover a long time range of isotope data, particularly from 2010 to 2020. During this period, methane concentration shifted from a previous equilibrium state to rapid growth, and isotope values significantly reversed from a previously maintained enrich level to more depleted values.

We selected 18 of these sites, as shown in the Fig. 8 . The selected stations' detail information is shown in table 3, together with our ISAMO station information.

2.6 Curve Fitting Methods and Seasonal decomposition

To explore seasonal cycles, we adopted NOAA Curve Fitting Methods (Thoning et al. [1989]), or called CCGCRV, which has been widely used in previous studies(Miller and Tans [2003], Ballantyne et al. [2010], ,Dowd et al. [2023]Woolley Maisch et al. [2023]). The main principle of this method is to decompose the original data into a function and residuals. The function part is composed of a polynomial and harmonics function. The polynomial part represents the average trend, which is shown

as the purple dash line in Fig. 9 b, while the harmonic function represents the mean seasonality, as the red dash line in Fig. 9 c.

For the residual part, the fast Fourier transform is used to transfer the time series to the frequency domain, a filter with a short-term cutoff is applied first to remove the shortest period component. By further applying a long-term cutoff on the remaining residuals, the long-term residuals and the median-term residuals will be separated. The smooth fit of trend and seasonality will be achieved by adding these residuals to the polynomial function and the harmonics part respectively, as the green and orange lines shown in Fig. 9 b and c. Combining them will give us the smooth fit of the raw time series, as the orange line in Fig. 9 a).

For the detailed parameter settings of NOAA curve fit method, we adopted the default settings in the python script provided by NOAA, that is, using a quadratic polynomial to represent the mean long-term trend and a four-term harmonics to represent mean seasonality. The expression of the function part is as follows:

$$\begin{aligned} y(t) = a + bx + cx^2 \\ + d_1 \sin(2\pi t) + e_1 \cos(2\pi t) \\ + d_2 \sin(4\pi t) + e_2 \cos(4\pi t) \\ + d_3 \sin(6\pi t) + e_3 \cos(6\pi t) \\ + d_4 \sin(8\pi t) + e_4 \cos(8\pi t) \end{aligned} \tag{2.7}$$

For short-term and long-term cutoff values, We used 80 and 667 days, which have been proven to be reasonable in previous studies (Umezawa et al. [2012], Woolley Maisch et al. [2023]). This means that residuals with a period of less than 80 days will be removed, and a period of 667 days will be used to separate seasonal residuals from long-term residuals.

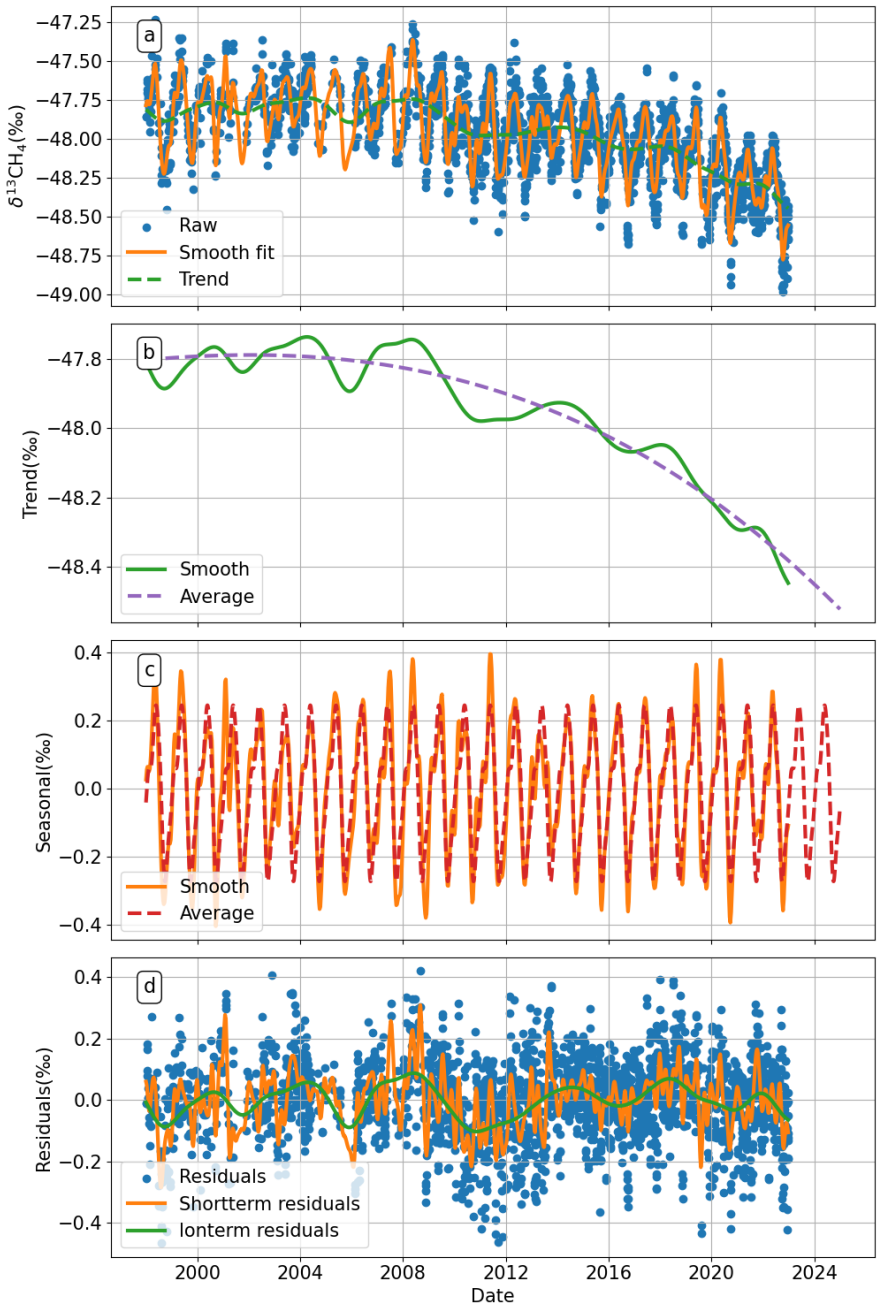

Figure 9: Example of NOAA curve fit on $\delta^{13}CH_4$ at BRW. a)Raw data with smooth trend and fit line b) Trend c) Seasonality d) Residuals

2.7 Isotopic discrimination —Miller & Tans method

The method for determining the source of carbon in the atmosphere was first introduced by Keeling, who found the variations in the carbon δ are proportional to the reciprocal of molar concentrationKeeling [1958].

Miller and Tans [2003] adopted the approximation of Tans [1980] that $\delta^{13}C \times CO_2$ is conserved. They then expressed the mass conservation equation as follows:

$$C_{\text{obs}} = C_{\text{bg}} + C_s \tag{2.8}$$

$$\delta_{\text{obs}} C_{\text{obs}} = \delta_{\text{bg}} C_{\text{bg}} + \delta_s C_s \tag{2.9}$$

By combining eq. (2.8) and eq. (2.9), They obtained a new equation:

$$\delta_{\text{obs}} = \frac{C_{\text{bg}}}{C_{\text{obs}}} (\delta_{\text{bg}} - \delta_s) + \delta_s \tag{2.10}$$

Based on the expression of eq. (2.10), when we assume that the isotope compositions of the background and the source are relatively stable, the equation can be seen as $\delta_{\text{obs}} = a/C_{\text{obs}} + b$ in linear form. By plotting the observed δ values against the inverse of the observed concentrations and performing linear regression, we can obtain the intercept, which represents the isotope composition of the source or sink. This is commonly used in isotope analysis called the Keeling plot.

This method is simple and reliable. However, there are some limitations. It assumes that the isotopic values of the background and the source are relatively stable. As can be seen in eq. (2.10), for a changing background, the slope $C_{\text{bg}}(\delta_{\text{bg}} - \delta_s)$ keeps changing, making it difficult to obtain an intercept on y-axis through linear regression.

Considering this,Miller and Tans [2003] rearranged the equation to obtain another expression of mass conservation:

$$\delta_{\text{obs}} C_{\text{obs}} - \delta_{\text{bg}} C_{\text{bg}} = \delta_s (C_{\text{obs}} - C_{\text{bg}}) \tag{2.11}$$

By plotting the difference of product of δ and concentration for observed and background values versus the difference of observed and background concentrations, the slope obtained from ordinary least squares regression (OLR) represents the source δ value, as shown in Fig. 10. This method has been applied in the analysis of atmospheric CO_2(Ballantyne et al. [2010]) and CH_4 (Umezawa et al. [2012], Woolley Maisch et al. [2023]) and their $\delta^{13}C$ time series.

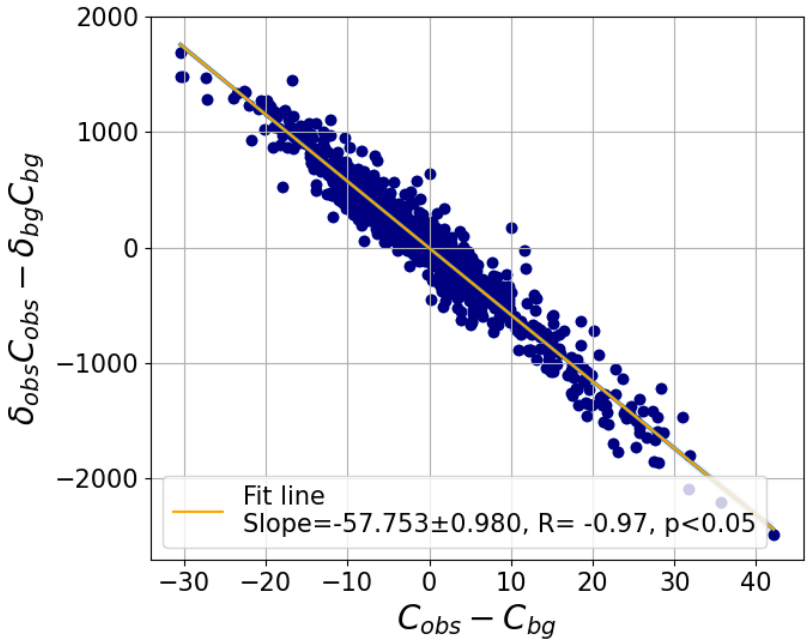

Figure 10: Example of Miller & Tans Plot at BRW

In fact, this is also a kind of signal decomposition. Since the time series of methane concentration and isotope composition in the real atmosphere consists of mixed signals, we can consider the observed

signal as a combination of background atmosphere, emissions, and sinks. Therefore, by choosing different backgrounds, we can obtain source information excluding the background.

If we use a smooth fit as the background, according to the CCGCRV method we applied (Thoning et al. [1989]), the resulting source δ value reflects regional short-term variability. Else, if we use the trend as the background, the source δ value also includes seasonality of two raw timeseries, representing processes on larger temporal and spatial scales superimposed on the regional signal.

For an explanation of the source, Miller and Tans [2003] described it with the following expression:

$$\delta_s = \frac{F_a\delta_a + F_b\delta_b}{F_a + F_b} \tag{2.12}$$

where the F represents the flux

This means that the source δ value obtained from the Miller & Tans plot is still a weighted average δ value from various sources.

2.8 Inverse model

There is still a lot of uncertainty in the global methane budget, especially the large gap between bottom-up and top-down estimates. Therefore, using only bottom-up methane emission data for analysis may not be enough to help us explain the seasonality of methane and its isotopes. Based on TM5-4DVAR, Basu et al. [2022] constructed an atmospheric inversion model. By also adding $\delta^{13}CH_4$ observation data to the CH_4 observation data for assimilation, the emission sources of methane in the atmosphere were better evaluated.

In this study, we used the output data from the inversion framework to compare and analyze the CH_4 and $\delta^{13}CH_4$ time series produced by the model from 1997 to 2017 with observational data. Additionally, we examined the monthly emission data generated by the model, which is categorized into three different sources: fossil, microbial, and pyrogenic. This analysis aimed to explore the relationship between seasonality of CH_4 and $\delta^{13}CH_4$ and emissions from these various sources.

3 Results

3.1 Methane isotope measurement at IMAU and comparison

3.1.1 $\delta^{13}CH_4$ measurement

Fig. 11 shows the IMAU measurement results of methane samples from four NOAA stations included in the BUDS project. The circles represent the long-term time series of $\delta^{13}CH_4$ from NOAA GML. The function part is fitted and extracted by NOAA CCGCRV to represent the trend and mean seasonality, which are represented by dashed and solid lines in the figure respectively. We extend it to the recent period through the function expression and intercept the part after 2020 for better display. The blue stars represent the measurement results of the same sample at INSTAAR laboratory. The quality control steps are shown in section 2.3. Both IMAU and INSTAAR data are added with offset to move to the standard of MPI. The specific offset values are shown in section 2.4.

In general, the measurements at IMAU can reproduce the results of INSTAAR well and are consistent with the average trend and seasonality of the long-term time series, which proves that the sample transfer method of INSTAAR is reliable, the sample reproducibility is good, and our assessment of the offset between the two laboratories is reasonable. However, for the stations in the southern hemisphere, especially the SMO station, our measurement results do not show clear seasonality because the seasonality of the station itself is very weak.

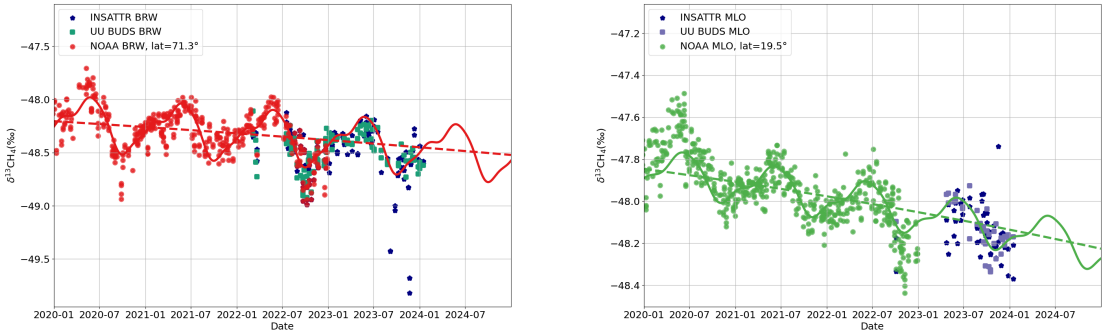

(a) BRW

(b) MLO

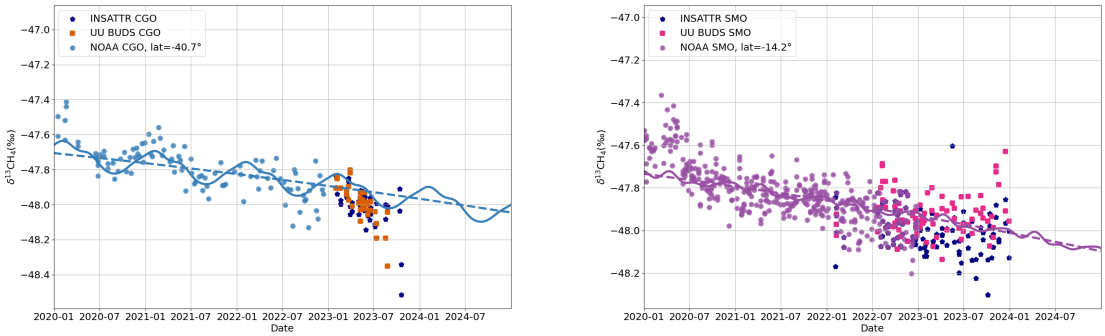

(c) CGO

(d) SMO

Figure 11: $\delta^{13}CH_4$ of BUDS, compared with INSTAAR and NOAA

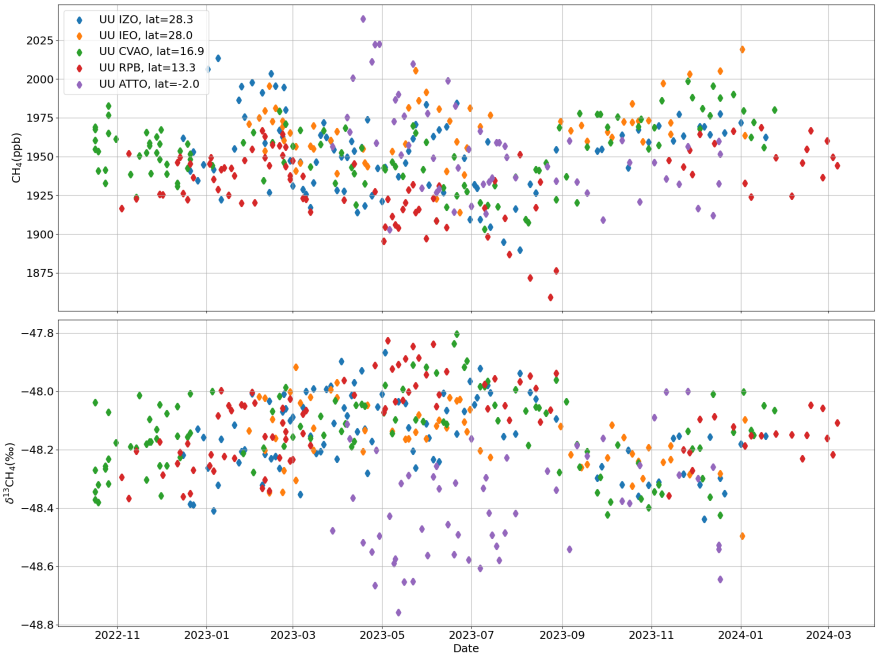

Figure 12: CH_4 (upper) and $\delta^{13}CH_4$ (lower) time series of ISAMO project

Fig. 12 shows our measurements of five ISAMO project sites. The four NH sites of $\delta^{13}CH_4$ show a

relatively complete seasonal cycle, i.e. enrichment in summer and depletion in autumn. However, we found that the $\delta^{13}CH_4$ for the tall tower observatory in the Amazon rainforest (ATTO) is not in line with the typical values in the SH, which are often more enriched than those in NH.

At our ISAMO sites, there is no long-term $\delta^{13}CH_4$ observation data from NOAA. For comparison, we selected the NOAA MLO station with a latitude close to four northern hemisphere sites and the NOAA ASC station in the southern hemisphere close to ATTO.

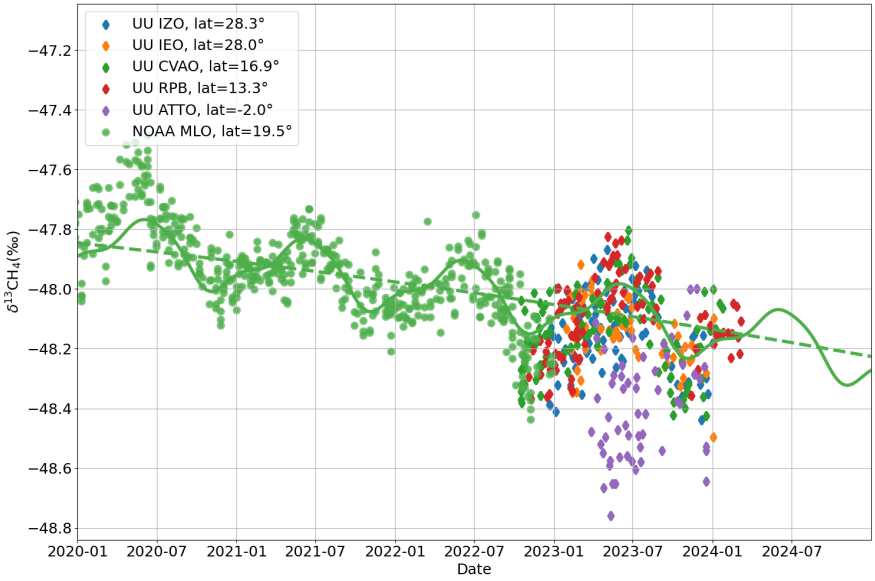

Figure 13: $\delta^{13}CH_4$ timeseries of ISAMO, compared with NOAA

In Fig. 13, We found that the trend and mean seasonality of the four NH stations are basically consistent with the MLO station, and can well reflect the peak in July and the trough in November. For ATTO, by comparing it with the southern hemisphere NOAA ASC with similar latitude, we found that it shows completely different characteristics from the southern hemisphere stations. Its average $\delta^{13}CH_4$ value and amplitude seem to be closer to the northern hemisphere BRW station. Although there may exist some errors, such a significant difference still indicates that there may be some mechanisms in the Amazon region that cause such a strong depletion of $\delta^{13}CH_4$.

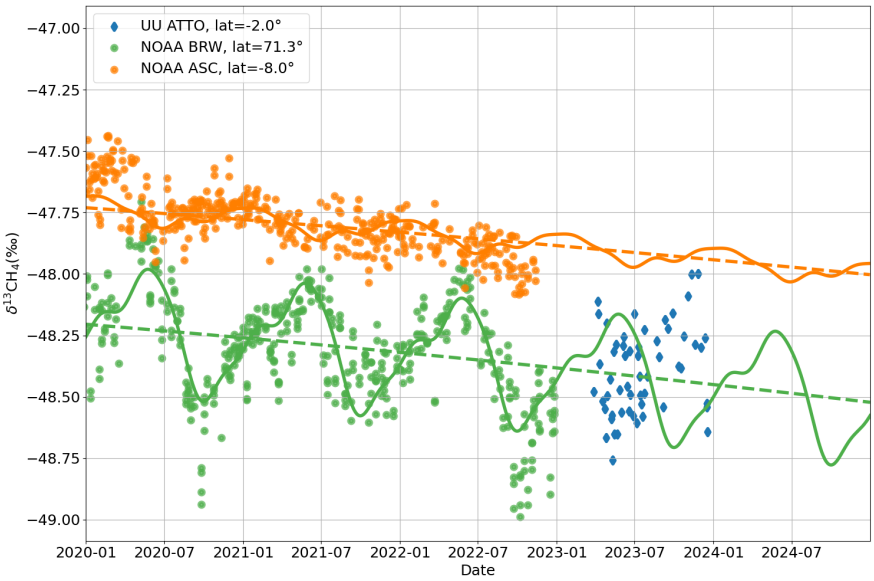

Figure 14: $\delta^{13}CH_4$ timeseries of ATTO, compared with NOAA ASC and BRW

3.1.2 $\delta D - CH_4$ measurement

At UU, our measurements of methane stable isotopes also include $\delta D - CH_4$. Fig. 15 summarizes our $\delta D - CH_4$ measurements, including long-term measurements at the Zeppelin station. As can be seen in Fig. 15, our $\delta D - CH_4$ measurements for BUDS agree well with the long-term time series of the Zeppelin station at similar latitudes.

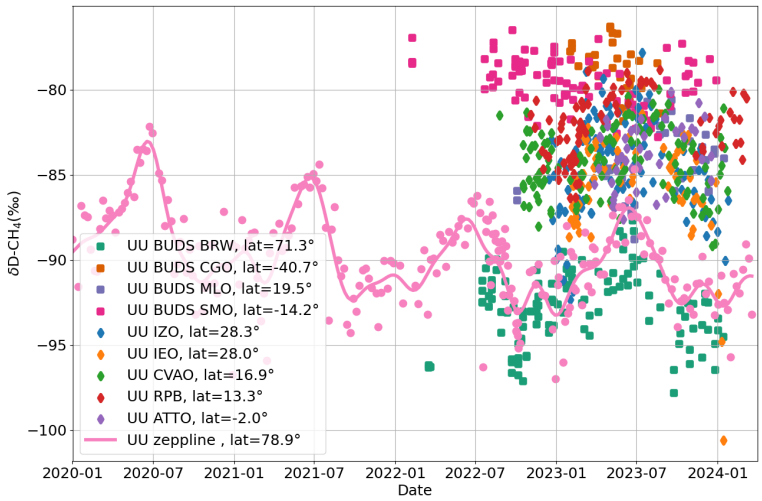

Figure 15: $\delta D - CH_4$ timeseries of IMAU project

Since NOAA's long-term measurements of $\delta D - CH_4$ stopped in 2009, it is difficult to compare our $\delta D - CH_4$ results with those of other laboratories. However, by using the $\delta D - CH_4$ characteristic lines that merge the northern and southern hemispheres, we can link past NOAA measurements with our more recent measurements for approximate comparison.

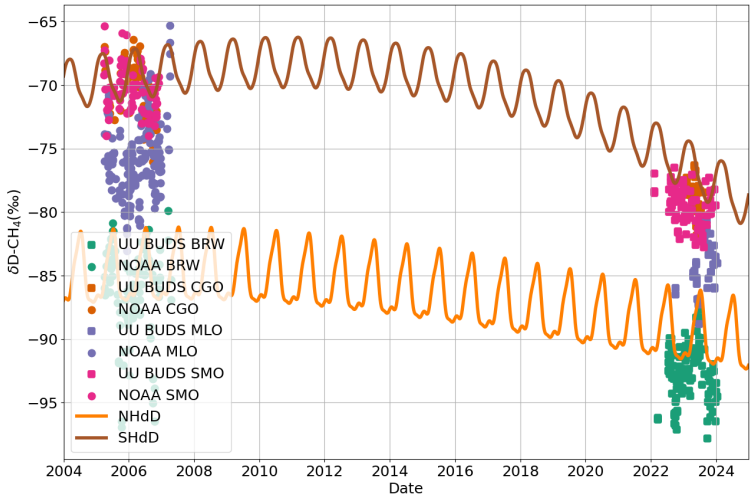

Figure 16: $\delta D - CH_4$ timeseries of IMAU project, connected by merged timeseries to compare with NOAA former data

As can be seen in Fig. 16, the two parts of the data can be well linked through the merged line. The $\delta D - CH_4$ we recently measured at the same site also conforms to the gradients and the average seasonal cycle at different latitudes, although there are still some offsets. This may be because the function part is not sufficient to fully represent the changes in $\delta D - CH_4$, or there are still some problems in the choice of offset.

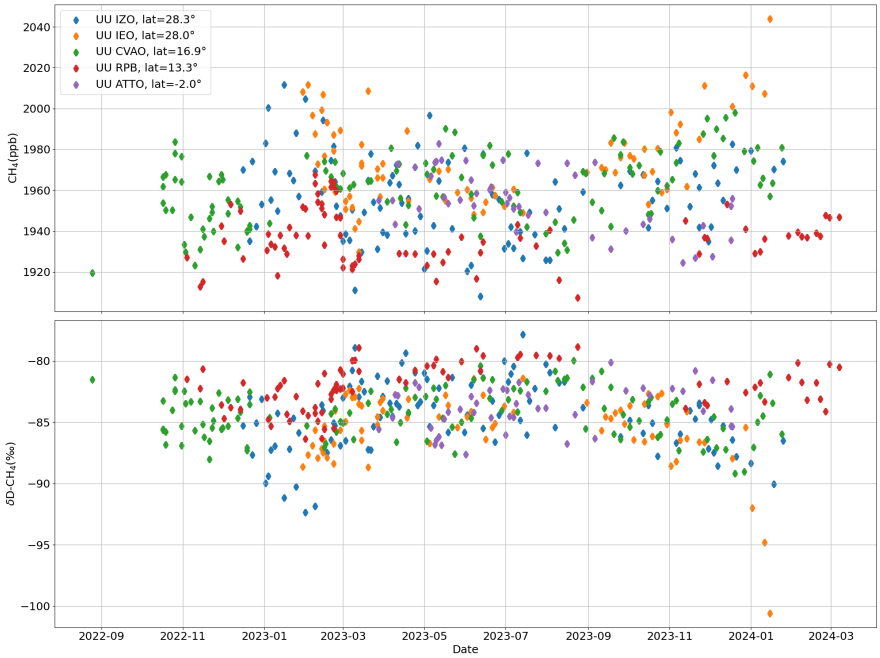

Figure 17: CH_4 (upper) and $\delta D - CH_4$ (lower) timeseries of ISAMO project

Similarly, we also measured $\delta D - CH_4$ at the ISAMO site, but we lacked long-term time series for comparison at the same site. It should be noted that in the $\delta D - CH_4$ measurement, unlike our previous measurement results for $\delta^{13}CH_4$, we did not find that the $\delta D - CH_4$ at the ATTO site were significantly different from those at other sites.

3.2 Seasonality of the global CH_4 and $\delta^{13}CH_4$ time series

Our measurements are highly accurate, but due to our measurement project started recently, we lack sufficient of data for seasonal analysis. Therefore, we analyzed the seasonality of CH_4 and $\delta^{13}CH_4$ data from NOAA's 18 long-term measurement sites in the next part.

3.2.1 Mean seasonal cycle at different sites

We first performed a seasonal decomposition on global methane and its isotope time series and extracted the function part, which reflects the average characteristics of the time series. We focus on the harmonic function part which is related to seasonality.

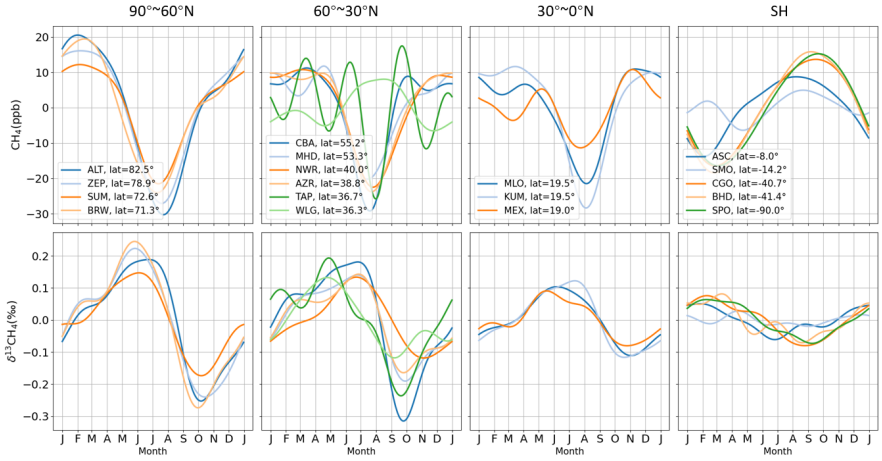

Figure 18: Mean seasonality of CH_4 (upper) and $\delta^{13}CH_4$ (lower) at NOAA stations

Fig. 18 shows the mean seasonal cycle of CH_4 and its $\delta^{13}CH_4$. It can be seen that CH_4 and $\delta^{13}CH_4$ show basically opposite seasonality in the SH, the maximum/minimum values of CH_4 correspond to the minimum/maximum values of $\delta^{13}CH_4$. The seasonal cycle shape is simple, especially for the mid and high-latitude stations in the SH, whose concentrations show the characteristics of a single harmonic function. This may because the southern hemisphere has less emissions compare to the NH, especially the high-latitude stations, whose seasonality is mainly dominated by OH oxidation.

In NH, the seasonal cycle shape is much more complex. The CH_4 reaches the lowest value in summer and the highest value in winter. At the same time, the $\delta^{13}CH_4$ is enriched in spring and reaches a peak in summer, and turns to depletion in autumn. The anti-correlation between CH_4 and $\delta^{13}CH_4$ is not obvious, especially there exists an autumn depletion of $\delta^{13}CH_4$, there is no corresponding methane maximum like in the SH. At the same time, the isotope maximum also seems to occur earlier than the minimum methane concentration. According to Spivakovsky et al. [2000], the OH concentration in the NH increases in summer and decreases in winter, while in the SH is the opposite. At the same time, the average concentration difference between the NH and SH is not large. The seasonality of OH can be used to explain the methane concentration and its $\delta^{13}CH_4$ seasonality (East et al. [2024]) in the SH. However, for the NH, the minimum methane concentration in summer lasts for a short time and is followed by a strong $\delta^{13}CH_4$ depletion effect in autumn. The OH sink alone cannot explain the complex seasonality of CH_4 and $\delta^{13}CH_4$ in NH, the complex emission distribution in the NH needs to be taken into account.

To more intuitively show the distribution of mean seasonality at various latitudes, we calculated the seasonal cycle amplitude, where the seasonal amplitude is represented by the maximum peak value minus the minimum valley value in the mean seasonal cycle.

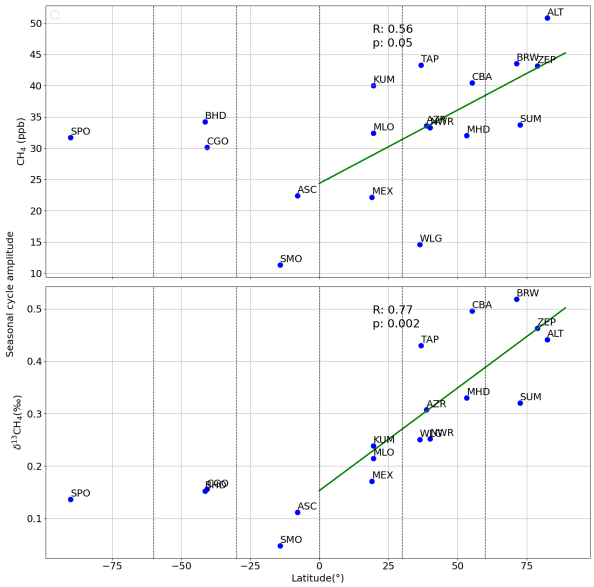

Figure 19: Latitude gradient of Mean Seasonal cycle amplitude

As can be seen from Fig. 19, in the NH, the seasonal cycle amplitude of CH_4 and $\delta^{13}CH_4$ increases with increasing latitude, especially for $\delta^{13}CH_4$.

For SH, there is no significant difference in the average seasonal amplitude of CH_4 and $\delta^{13}CH_4$ in mid- and high-latitudes. This is reasonable considering the small amount of emissions

3.2.2 Inter-annual Trend of Seasonal Cycle Amplitude

Dowd et al. [2023] analyzed the seasonality of CH_4 data from NOAA GML. We used the same method to reanalyze the latest version data, we also conducted the same analysis on $\delta^{13}CH_4$ data.

For CH_4, we obtained similar results, that is, in the high latitudes of the NH, the seasonality of methane concentration showed a downward trend. At the same time, the SH stations and northern mid and low-latitude stations showed upward trends. The results were not significant ($p > 0.05$) for most stations, except for the following: BRW and ZEP in the NH high-latitude; NWR and MLO in the NH mid and low-latitude; and ASC, CGO, and SPO in the SH.

When we combined our results with Fig. 19, we found that these insignificant stations also seemed to behave like "outliers" in terms of mean seasonality, so it can be assumed that these stations may be affected more by local scale factors rather than showing a more general feature of within its latitude range.

In summary, although the method of using the difference between the maximum and minimum values to reflect the seasonal amplitude is relatively rough and the correlation is not high, we believe that it still reflects the basic trend of some large-scale seasonal changes in methane concentrations on a global scale, that is, due to the rapid growth of global methane and more atmospheric methane is affected by OH sink, the global methane seasonal cycle amplitude shows an upward trend (Dowd et al. [2023]). However, this is not the case in the high latitudes of the NH.

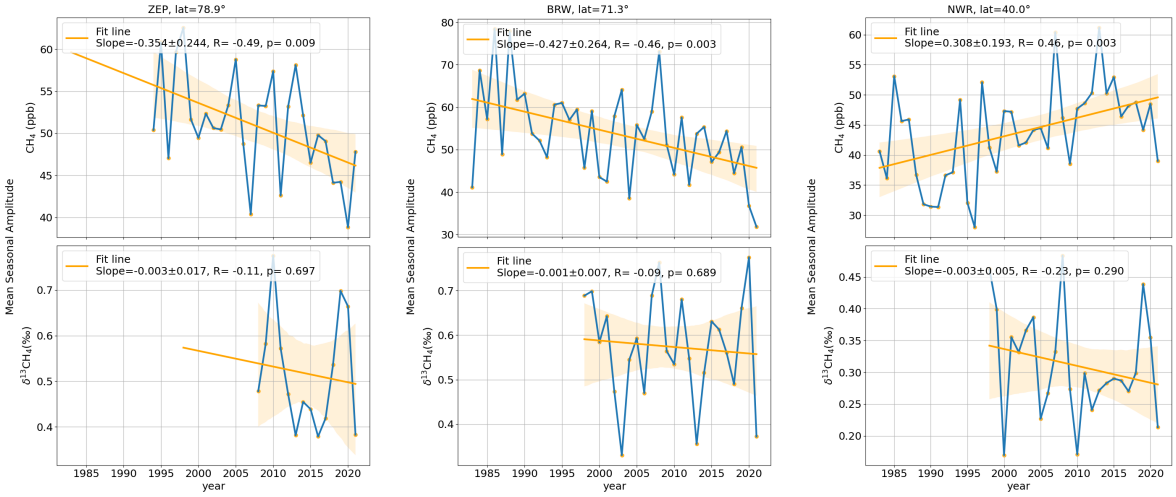

(a) ZEP (b) BRW (c) NWR

(d) MLO (e) CGO (f) SPO

Figure 20: Inter-annual Trends of mean seasonal cycle amplitude

For this result, Barlow et al. [2016] suggests that this is due to the enhanced emissions from high-latitude wetlands. The enhanced emissions from wetlands in summer will increase the seasonal minimum of methane, thereby reducing the amplitude. Dowd et al. [2023] reproduced the changes in the seasonal amplitude of methane through the TOMCAT model and attributed them. They believe that this may be caused by the combined effects of emissions and transport in low-latitude areas and emissions in high-latitude areas.

By conducting a similar analysis on $\delta^{13}CH_4$, we hope to obtain information on the seasonality of methane isotopes to further confirm the conclusions of Barlow et al. [2016] and Dowd et al. [2023]. Unfortunately, we did not find a significant inter-annual trend of seasonal cycle amplitude in the analysis of $\delta^{13}CH_4$, the p-values of all stations are larger than 0.05.

3.3 Source $\delta^{13}CH_4$ by Miller & Tans analysis

3.3.1 Overview of source $\delta^{13}CH_4$ of stations

In the previous section, we analyzed the $\delta^{13}CH_4$ time series but did not get significant results. Since the time series is a time series with mixed $\delta^{13}CH_4$, the analysis of it cannot reflect the source $\delta^{13}CH_4$ information. Therefore, we consider using the Miller & Tans method to analyze the source $\delta^{13}CH_4$.

For specific methods, see section 2.7.

We used two different backgrounds to perform Miller & Tans analysis. The background here is actually not the background concentration corresponding to emissions in common sense. Since the NOAA measurement stations are already atmospheric background measurement stations, the background here is more of a signal that we want to remove. Therefore, its selection can be arbitrary, depending on what information we want to obtain.

Specifically, here, by using smooth fitting from CCGCRV as the background, we actually obtain the source $\delta^{13}CH_4$ of the shortest component in the observation data, or in other word, the regional scale source $\delta^{13}CH_4$. While using the deseasonalized trend as the background, we obtain the superposition of the source $\delta^{13}CH_4$ of the shortest component and the seasonal component, which includes more processes, such as atmospheric mixing and transport on a larger spatial and temporal scale and the influence of sink.

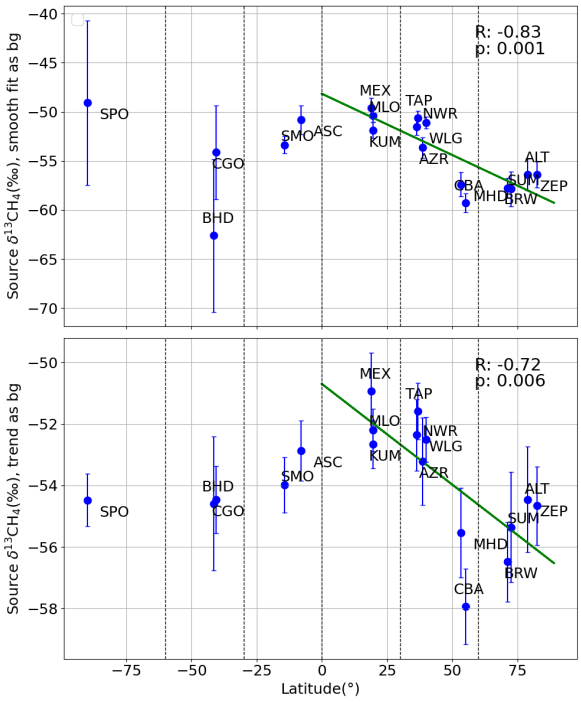

Figure 21: latitude gradient of isotope source composition, Smooth fit as background (upper), Trend as background (lower)

First, we performed a Miller & Tans analysis on the complete time series of each station. As shown in the Fig. 21, the background used for creating the upper plot is the smooth fit, and the background of the lower plot is the trend. In the NH, we can see that there is an obvious latitude gradient in the source $\delta^{13}CH_4$, especially when we use smooth fit as the background, which reflects more local scale information. We can see the depleted source $\delta^{13}CH_4$ in the high latitudes of the NH. This is caused by the depletion $\delta^{13}CH_4$ of high-latitude wetlands and relatively less fossil emissions. In contrast, the relatively enriched $\delta^{13}CH_4$ in the mid and low latitudes are related to the fossil and pyrogenic emissions in these areas.

At the same time, according to previous research, the $\delta^{13}CH_4$ of the wetland itself also has a latitude gradient. The $\delta^{13}CH_4$ of the tropical wetland are enriched approximately 11‰ compared to the NH high-latitude wetlands (Ganesan et al. [2018], Oh et al. [2022]).

From the lower plot inFig. 21 , it can be seen that after introducing a larger scale transport and mixing processes, the source $\delta^{13}CH_4$ gradient has a certain reduction, from 12‰ to about 6‰, but there is still a clear difference between low and high latitudes.

As for the SH, due to low emissions and other reasons such as measurement problems, makes the source $\delta^{13}CH_4$ derived from short-term variations not very reliable with large error ranges. However, after introducing the seasonal component, their source $\delta^{13}CH_4$ are basically around -54‰, which are close to the global averaged source $\delta^{13}CH_4$, as shown in Fig. 1.

3.3.2 Mean seasonality of source $\delta^{13}CH_4$

Since we used two different backgrounds, in which the smooth fit contains seasonal components in the background, intuitively, using this background may remove seasonality from the remaining signal, resulting in the source $\delta^{13}CH_4$ not containing seasonality.

Therefore, we classified the multi-year data of each station by month, and performed Miller & Tans analysis on the data of each month to obtain the monthly source $\delta^{13}CH_4$, and analyzed their mean seasonality to verify whether the source $\delta^{13}CH_4$ obtained using smooth fit can still correctly express seasonality.

From Fig. 22, we can see that the results of several representative stations, the mean seasonality of source $\delta^{13}CH_4$ obtained by smooth fit and the trend as the background shows similar seasonality, which can prove to some extent that the source $\delta^{13}CH_4$ we obtained from smooth fit, that is, the regional source $\delta^{13}CH_4$, occupies a certain dominant position in the seasonality of source $\delta^{13}CH_4$.

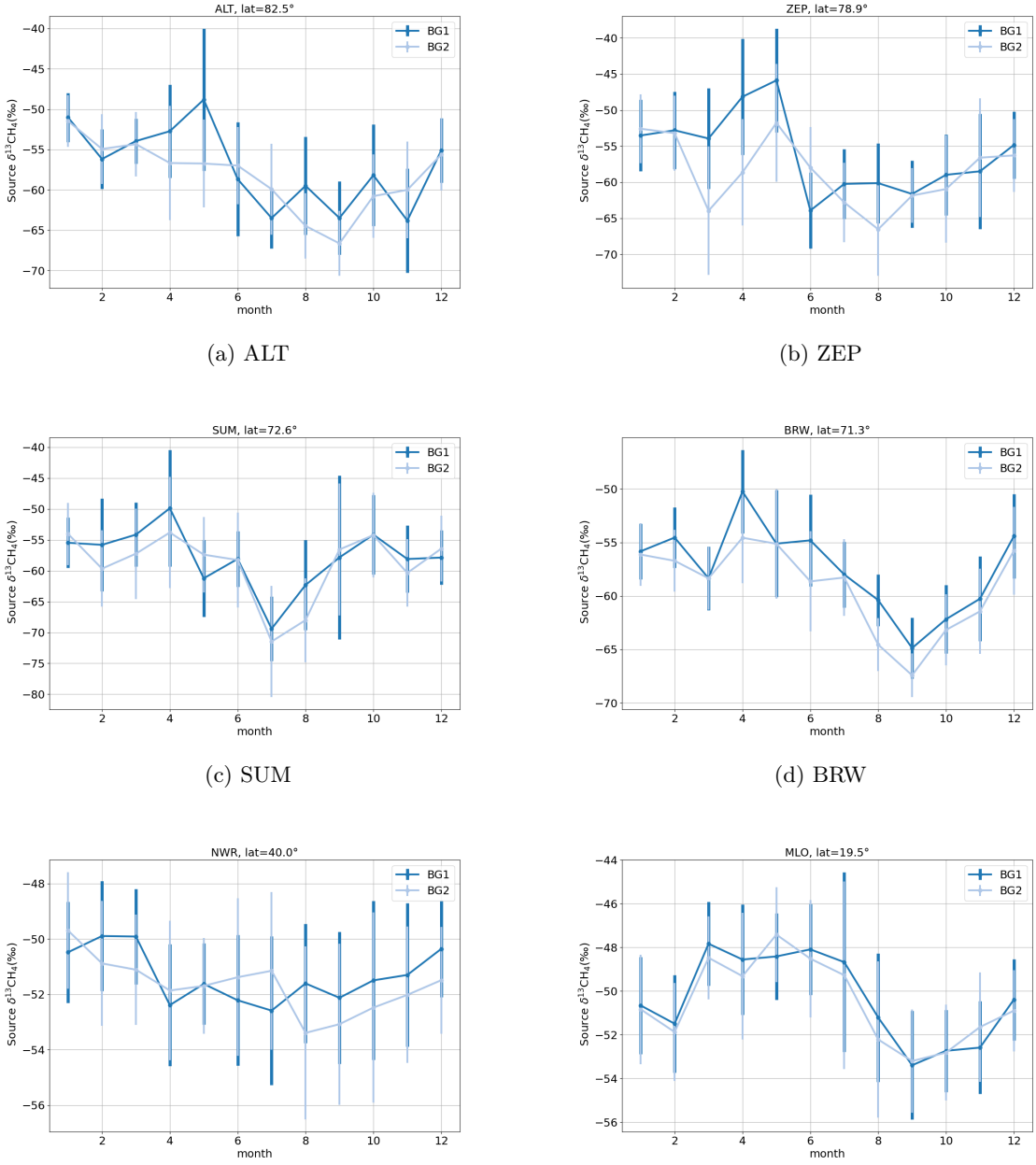

(a) ALT (b) ZEP

(c) SUM (d) BRW

(e) NWR (f) MLO

Figure 22: Mean seasonality of source $\delta^{13}CH_4$. BG1:smooth fit as background, BG2: Trend as background

3.3.3 Inter-annual variability of source $\delta^{13}CH_4$

Similar to the study of seasonal amplitude, we hope to explore the inter-annual variation of source $\delta^{13}CH_4$. We assume that due to the enhancement of high-latitude wetland emissions, according to eq. (2.12), the proportion of depleted $\delta^{13}CH_4$ increases, and the source $\delta^{13}CH_4$ will show a downward trend.

We grouped the time series by year and performed Miller & Tans analysis on each year to obtain the annual source $\delta^{13}CH_4$. Among them, due to the uneven distribution of data at each station each year, we screened the results of the analysis. If there are less than 10 data points used for Miller & Tans analysis in that year, or the result of linear regression is not significant (R<0.8, P>0.05), we will

exclude that year from the analysis results.

In section 3.2.2, we found that the seasonal cycle amplitudes of methane in the NH high latitudes is significantly different from other latitudes range of the world. At the same time, due to the low emissions and possible measurement errors, the slope error range obtained by Miller & Tans analysis in the SH is very large. Hence we focus on the result of several NH high latitude stations here.

We show the results of four high-latitude stations and also show NWR and MLO as representatives of mid and low-latitude stations for comparison. The results for the remaining stations can be found in the Appendix

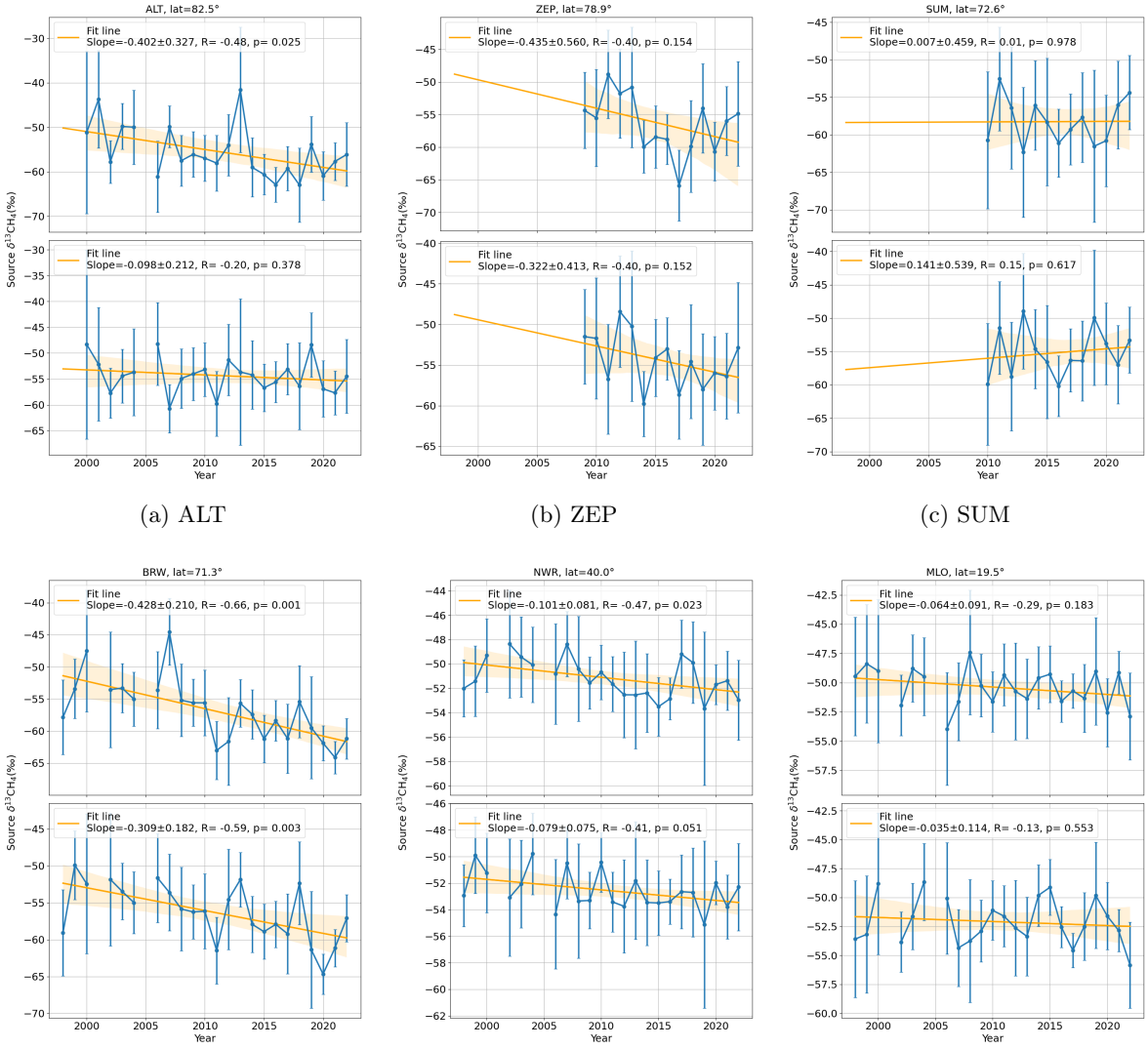

(a) ALT (b) ZEP (c) SUM

(d) BRW (e) NWR (f) MLO

Figure 23: Inter-annual Trend of source $\delta^{13}CH_4$. BG1(upper), BG2(lower)

From Fig. 23, we can see that when using smooth fit as the background, the source $\delta^{13}CH_4$ of high-latitude stations in the NH all show a downward trend. In comparison, the trends of NWR and MLO are also downward but with smaller slopes.

In the analysis using trend as background, except for BRW, the results of each station are even less significant, which is similar to our previous analysis of amplitude, which means that the introduction of larger-scale processes and sinks brings more uncertainty to the inter-annual change of the source $\delta^{13}CH_4$.

Based on the inter-annual trend obtained by smooth fitting as the background, we found that in most areas of the Northern Hemisphere, the regional scale source $\delta^{13}CH_4$ show a downward trend, especially in high-latitude stations such as ALT and BRW, the regional scale source $\delta^{13}CH_4$ value experienced a decrease of about 10‰, moving to more depleted $\delta^{13}CH_4$. However, for NH high-latitude wetlands, their $\delta^{13}CH_4$ should be more depleted, about -67.8‰(Ganesan et al. [2018]). This is reasonable because we get a mixed signal, and there may be a certain degree of fossil emission influence, which makes the mixed source $\delta^{13}CH_4$ value a bit richer, but the depletion of the source $\delta^{13}CH_4$ still shows that the flux proportion of the more depleted emission is gradually increasing. In SUM and ZEP, we can observe similar situations. However, this is accompanied by large uncertainties. This may be related to the relatively short of $\delta^{13}CH_4$ time series.

For NH low and mid-latitudes, this depletion is less obvious, which is reasonable considering the fossil emissions in mid-latitudes and the spatial distribution of $\delta^{13}CH_4$ of wetland emission(Ganesan et al. [2018]), which also means that we may underestimate the increase of fossil and pyrogenic emissions in low and mid-latitudes due to the enhancement of the more depleted microbial signal.

3.4 Inverse model result analysis

Since there is still a lot of uncertainty in the global methane budget, especially the large gap between bottom-up and top-down estimates, using only bottom-up methane emission data for analysis may not be enough to help us explain the seasonality of methane and its isotopes(Kangasaho et al. [2022]).

Here, we used the output data of the inversion framework provided by Basu et al. [2022], and made a simple comparison and analysis of the methane and isotope time series output by the model from 1997 to 2017 with the observational data.

3.4.1 Time series comparison between Model and observation

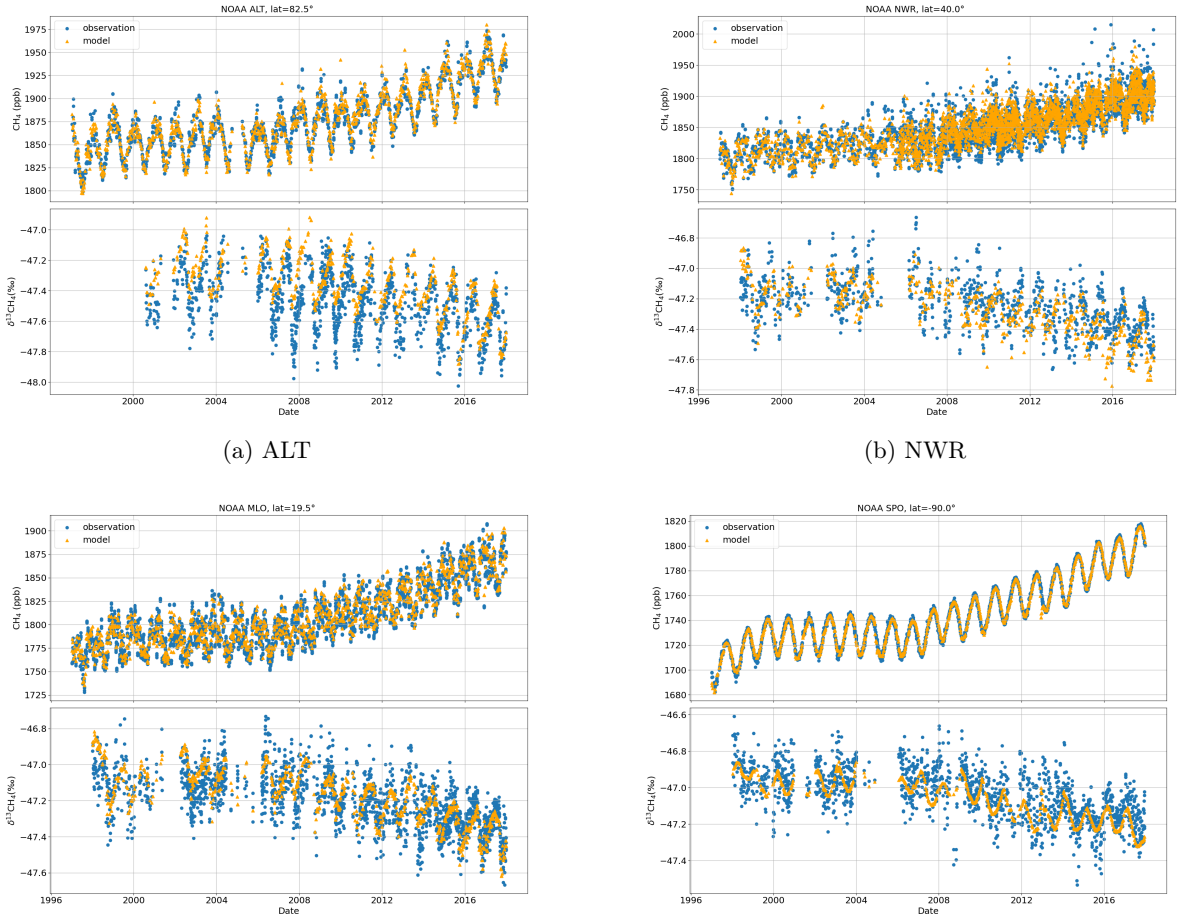

(a) ALT

(b) NWR

(c) MLO

(d) SPO

Figure 24: 1997-2017 CH_4 and $\delta^{13}CH_4$ from Inverse model output and observation

In Fig. 24, we found that the model output can well reproduce the long-term trend and seasonality of atmospheric CH_4. However, although the addition of $\delta^{13}CH_4$ data for assimilation can well reproduce the mean level and long-term trend of $\delta^{13}CH_4$ at most stations, the model overestimates the level of $\delta^{13}CH_4$ for high latitudes in the Northern Hemisphere.

The seasonality of CH_4 and $\delta^{13}CH_4$ are compared between the model and observation by using the smooth seasonal cycle extracted from NOAA CCGCRV.

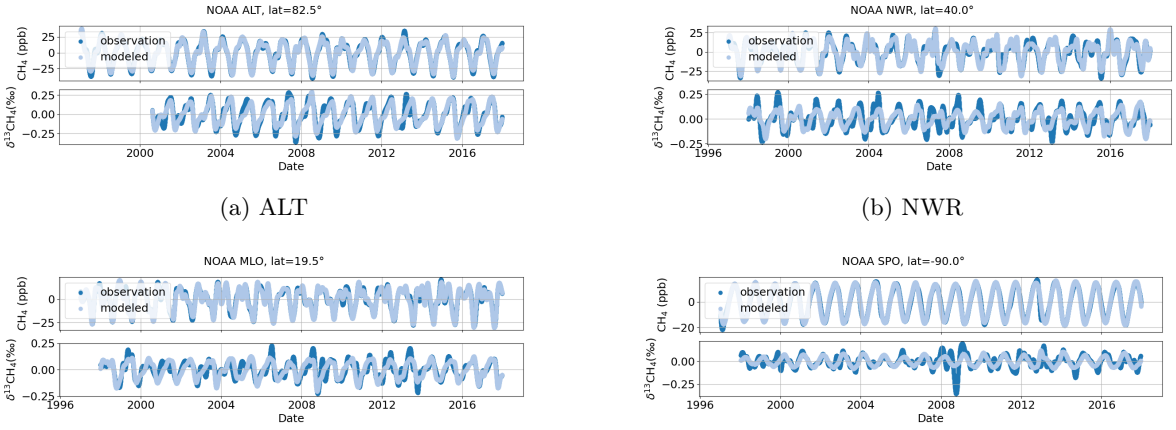

(a) ALT

(b) NWR

(c) MLO

(d) SPO

Figure 25: 1997-2017 smooth cycle of CH_4 and $\delta^{13}CH_4$ from Inverse model output and observation

At the same time, for the seasonal cycle of $\delta^{13}CH_4$ shown in Fig. 25, the model underestimates the amplitude of the seasonal component to a certain extent, which shows that there are still some problems in the model's classification of different sources.

3.4.2 Source specific emissions information from Model

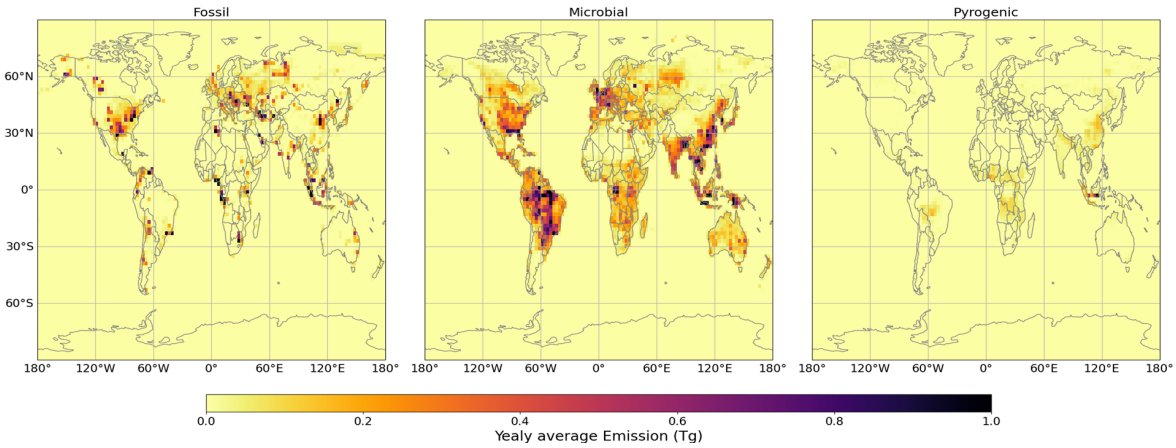

Figure 26: Posterior yearly averaged specific source emission from inverse model

Fig. 26 shows the distribution of yearly average emissions from three different sources. We found that fossil sources are mainly concentrated in the middle and low latitudes of the Northern Hemisphere, mainly in North America, Europe and Asia. In contrast, microbial sources are more widely distributed and more intense. Pyrogenic emissions are the least and are mainly concentrated in East Asia and areas near the equator.

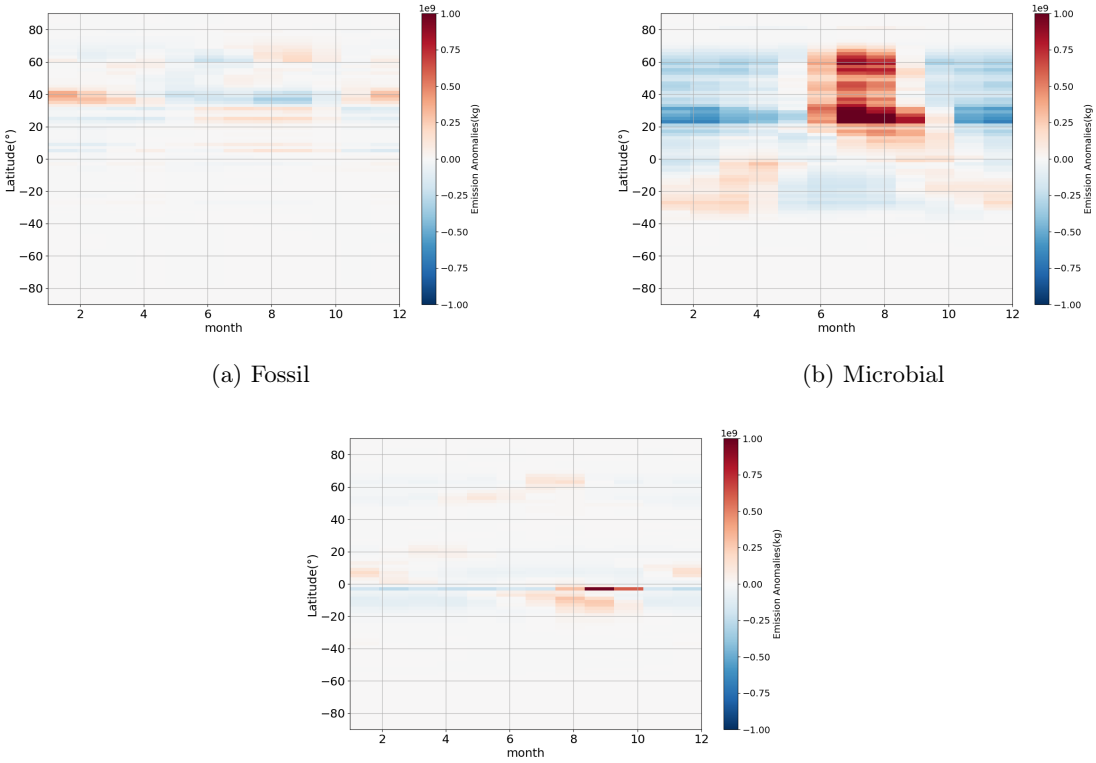

(a) Fossil

(b) Microbial

(c) Pyrogenic

Figure 27: Emission Anomalies of inverse model

Also, the mean seasonality of emission data in the model is analyzed. We detrended the emission data output of the inverse model and obtained the multi-year averaged emission anomalies of three emission sources. As can be seen in Fig. 27, the emission from fossil sources is mostly located in the northern hemisphere, showing the characteristics of summer enhancement and winter weakening in the middle and low latitudes (0-30°N), and the characteristics of summer weakening and winter enhancement in the area around 40°N. In the higher latitudes, there are similar characteristics but not obvious. For pyrogenic, there is strong autumn emission near the equator, and the seasonality in other regions is not obvious. Compared with the emission from microbial sources has obvious seasonal characteristics in a large range, especially in the area of 20°N to 30°N and 50°N to 60°N, there is an obvious summer enhancement and winter weakening.

Since wetland emissions often contain depleted isotope signature, after superimposing on the other two emissions that do not have obvious seasonality, it can be considered that the seasonality of the overall emission has an obvious wetland isotope signature, which is consistent with observation and the source $\delta^{13}CH_4$ obtained by Miller & Tans insection 3.3.2.

3.4.3 Mean seasonality of source $\delta^{13}CH_4$ in model

Similar to section 3.3.2, we applied the same approach to the model data to explore the mean seasonality of source $\delta^{13}CH_4$ in model and compared it with the results from the observational data.

From Fig. 28, we can see that for the four northern high-latitude stations, the model seems to underestimate their seasonality, which is reflected in smaller amplitudes, later minimum occurrence times, and earlier return enrichment levels in autumn. For the mid- and low-latitude stations, the model overestimates their mean source $\delta^{13}CH_4$ and seasonal amplitudes.

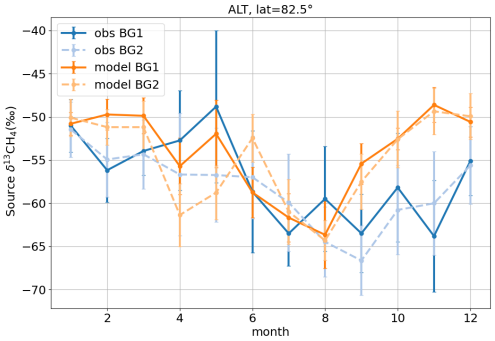

(a) ALT

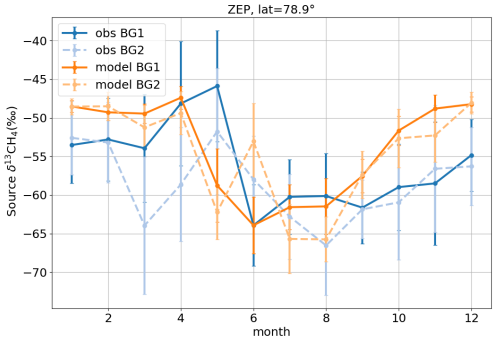

(b) ZEPmodel

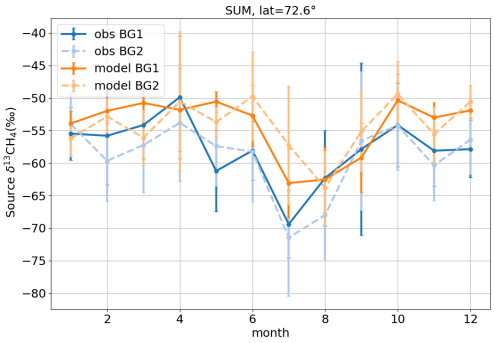

(c) SUMmodel

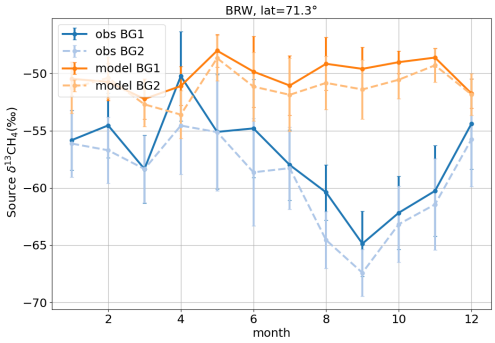

(d) BRWmodel

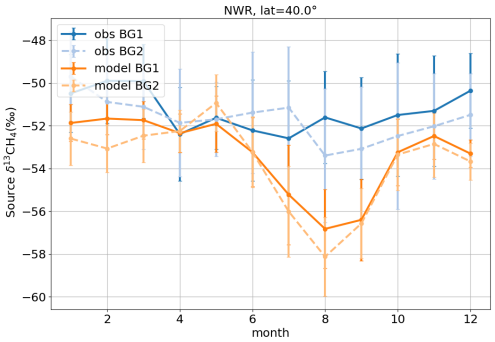

(e) NWRmodel

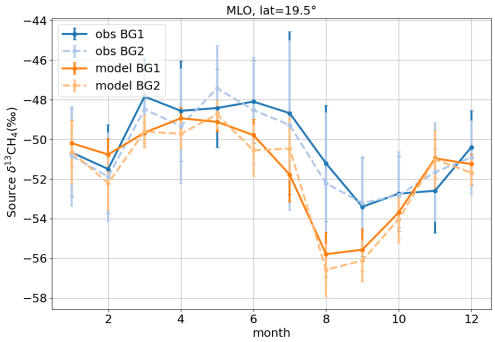

(f) MLOmodel

Figure 28: Mean seasonality of source $\delta^{13}CH_4$ in the inverse model, compared with observation result

4 Discussions

4.1 Limitations of quality control and data cleaning methods

In the first part, we show the methane isotope data measured at IMAU laboratory. Although we applied some quality control methods(Fig. 7) to eliminate outliers in the data as much as possible, there are still some data points that may be considered outliers.

First, for the problem of leakage or contamination during the transportation of samples, in the BUDS project, since NOAA uses a pair of flasks for each sampling, they can be compared with each other to minimize such problems. At the same time, we can identify the problematic sample bottles as much as possible and exclude them from the analysis by comparing with the $\delta^{13}CH_4$ measurement data

of INSTAAR. However, for the ISAMO project, we only have isolated flasks for measurement, and the content is low, which makes it difficult to repeat the measurement. Therefore, this brings some uncertainty and difficulty in reproduction.

In the NOAA dataset, the method they use to deal with outliers is to compare the data with smooth fit obtained by NOAA CCGRV(section 2.6), and the data exceeding 3σ are considered outliers. However, for the measurement data we currently have, the time series is too short to perform a complete seasonal decomposition and smooth fitting. Therefore, we arranged the data measured in the IMAU laboratory according to the sampling time and used the moving MAD method to clean up the outliers, but this has certain limitations.

First, the moving window is not effective for data on both edges of the time series. For data points at the edge only one side of the data is included in the window for calculation, it is likely to cause large errors in the calculation of its statistical value. Since our data interval sampling is relatively sparse, and there are problems such as transportation damage and instrument failure, the time series finally obtained for data cleaning may have a problem of few data points in a window, which will make the error range very large, so that possible outliers are regarded as normal values.

Although there are still some problems, we found that when comparing our measurement data with NOAA, it still fits the seasonality of NOAA's long-term series very well. Therefore, we believe that the data cleaning is basically effective, but in the future, after obtaining more data and a longer time range, the data cleaning method can be further improved.

4.2 Mean Seasonality of CH_4 and $\delta^{13}CH_4$

In the previous analysis, we found that by analyzing the time series of CH_4 and $\delta^{13}CH_4$ data at 18 NOAA observation stations, both have obvious mean seasonal characteristics.

In the northern hemisphere, CH_4 reaches its lowest value in the summer, while $\delta^{13}CH_4$ reach their highest value in the early part of the year and lowest values in the autumn (Kangasaho et al. [2022]). In the Southern Hemisphere, CH_4 and $\delta^{13}CH_4$ seasonality show opposite variation characteristics, while in the NH, the anti-correlation between the mean seasonality of CH_4 and $\delta^{13}CH_4$ is not obvious. Tyler et al. [2007] believes that this is due to the relatively small KIE of OH. According to Spivakovsky et al. [2000], OH in the NH reaches its maximum concentration in summer, which is reflected in the minimum value of CH_4. However, for $\delta^{13}CH_4$, according to Saueressig et al. [2001], under experimental conditions, OH has an effect on $\delta^{13}CH_4$:+0.002‰/ppb, while according to Morimoto et al. [2006]'s calculations, emissions from fossil and wetland sources will have an effect on $\delta^{13}CH_4$ about +0.004‰/ppb and -0.007‰/ppb, respectively. This KIE difference makes the seasonality of $\delta^{13}CH_4$ in the NH more affected by emission sources than the seasonality of OH(Tyler et al. [2007]).

Combining the seasonality of emissions from different sources obtained from the model (Fig. 27), we found that for the NH, the seasonality of microbial emissions is significantly stronger than the other two emissions, and its seasonality also agrees with the mean seasonality of the $\delta^{13}CH_4$ time series inFig. 18. When emissions are enhanced in July, the seasonal cycle of $\delta^{13}CH_4$ begins to decline from the maximum value until it reaches the minimum value in October later, when the emission intensity weakens and $\delta^{13}CH_4$ increases again.

Combined with the source $\delta^{13}CH_4$ information we obtained through Miller&Tans (Fig. 22), the seasonality shapes of source $\delta^{13}CH_4$ in the NH are also consistent with the seasonality of microbial emissions. Although the seasonal minimum values of source $\delta^{13}CH_4$ all appear earlier than the minimum values of the observed $\delta^{13}CH_4$ time series. Considering that it takes a certain amount of mixing time for emissions to enter the background atmosphere, this is reasonable.

Kangasaho et al. [2022] simulated $\delta^{13}CH_4$ using the TM5 model, EDGAR v5.0 emission data and process-based terrestrial ecosystem models and reached a similar conclusion that wetland emissions are the main factor affecting the seasonal cycle of $\delta^{13}CH_4$, although in their simulations, the model underestimated the seasonal cycle of each site and could not reproduce the depletion of $\delta^{13}CH_4$ in autumn well.

Comparing the seasonality of source $\delta^{13}CH_4$ obtained by using two different backgrounds, we found that the seasonal shapes obtained under the two backgrounds are similar, corresponding to the sea-

sonality of microbial emissions in the NH, indicating that on a regional scale, source $\delta^{13}CH_4$ in the NH is dominated by regional microbial emissions. At the same time, this feature still exists in the second background when larger-scale mixing and transport are introduced, and for northern mid and high-latitudes, the minimum value is a bit lower than that of regional source $\delta^{13}CH_4$, and the phase difference between each station is smaller, indicating that this microbial characterized seasonality is a common feature of the northern high latitudes.

In summary, for the mean seasonality, we conclude that in the Southern Hemisphere, the seasonality of the CH_4 and $\delta^{13}CH_4$ time series is dominated by the OH sink. In the Northern Hemisphere, OH still has a greater effect on the seasonality of CH_4. While for $\delta^{13}CH_4$, emissions play more important roles, especially microbial emissions, which dominate the regional source $\delta^{13}CH_4$ and affect its seasonality on a larger scale and background atmospheric observations through transport and mixing.

4.3 Explanation of several latitudinal gradients

After analyzing the average seasonal amplitude of each station, it was found that in the northern hemisphere, the mean seasonal amplitude of $\delta^{13}CH_4$ has a significant latitudinal gradient(Fig. 19), while in the southern hemisphere, it presents almost the same amplitude.

This may be caused by different emission sources. According to Fig. 26, for the southern mid and high-latitude, there are almost no emissions, and their seasonality is mainly dominated by OH, so they present almost consistent mean seasonal cycle characteristics; for the northern mid and low-latitude, there are more fossil emissions than in high-latitude regions. Compared with microbial sources, fossil source emissions have weaker seasonality, which will result in a smaller seasonal amplitude of atmospheric $\delta^{13}CH_4$ time series .

The source $\delta^{13}CH_4$ obtained from the two backgrounds also showed obvious latitudinal gradients (Fig. 21). Among them, the $\delta^{13}CH_4$ obtained with smooth fitting as the background shows a larger latitudinal gradient of about 11‰, while the source $\delta^{13}CH_4$ with the long-term trend as the background shows a smaller gradient of about 5‰ and shows almost the same characteristics in the southern hemisphere. This is because the source isotopes with smooth fitting as the background showed more regional characteristics, while the isotope signals with the long-term trend as the background introduced mixing and transport on a longer time and spatial scale, together with some sink effect. For the SH, this makes the source $\delta^{13}CH_4$ at each station eventually close to the global average source $\delta^{13}CH_4$ value of -54‰(Sherwood et al. [2017]).

Combined with the latitudinal gradient of the previous seasonal amplitude, this further proves that the distribution of emissions from different sources leads to the generation of latitudinal gradients. However, even for emissions from the same source, its isotopic composition itself has distribution characteristics. For example, compared with tropical wetlands, the $\delta^{13}CH_4$ of high-latitude wetlands is depleted by about 11‰ (Ganesan et al. [2018], Oh et al. [2022]), according to Sherwood et al. [2017], it can also be seen from Fig. 1 that the $\delta^{13}CH_4$ of the same source also has a large range of variation. Therefore, the spatial distribution of $\delta^{13}CH_4$ is also an important reason.

4.4 Inter-annual Trend

For the inter-annual variation of seasonal cycles, we used the method of subtracting the minimum value from the maximum value to analyze the CH_4 and $\delta^{13}CH_4$ time series. We found that the annual seasonal amplitude of CH_4 at seven stations had a significant interannual variation trend ($p<0.05$), among which the high-latitude stations in the north showed a downward trend, which is similar to the previous research results.Barlow et al. [2016] performed an experiment in TM5 model and found that only with increasing boreal wetland emission can the model agree with the observation.Dowd et al. [2023] use 3D chemical transport model, TOMCAT and surface observation to believe that this is mostly due to the emission and transportation from low latitudes.

However, for the seasonal amplitude of $\delta^{13}CH_4$, no significant inter-annual variation was found, which may be affected by multiple factors. For northern mid and high-latitudes, we assume that wetland emissions are enhanced, and the depleted $\delta^{13}CH_4$ is expected to reduce its seasonal minimum. In order to prevent the final seasonal cycle amplitude from changing significantly, its maximum value must

be reduced accordingly, which includes a variety of possibilities: weakening of the KIE of the sink, weakening of fossil emissions with enriched $\delta^{13}CH_4$ in winter and spring, or global warming may cause high-latitude wetland emissions to start earlier, directly affecting the maximum value of the seasonal cycle. Among them, Dowd et al. [2023] found reduced winter emissions in Canada, Europe, and the Middle East in the TOMCAT model, and these regions all contributed to the decrease in the seasonal amplitude of CH_4 in the high-latitude NH region, which may explain why the seasonal amplitude of the corresponding $\delta^{13}CH_4$ did not change significantly. Yuan et al. [2024] found that Boreal–Arctic regional wetland methane emissions have increased significantly because of climate change, which mostly happened in early summer. But more direct evidence is still needed.

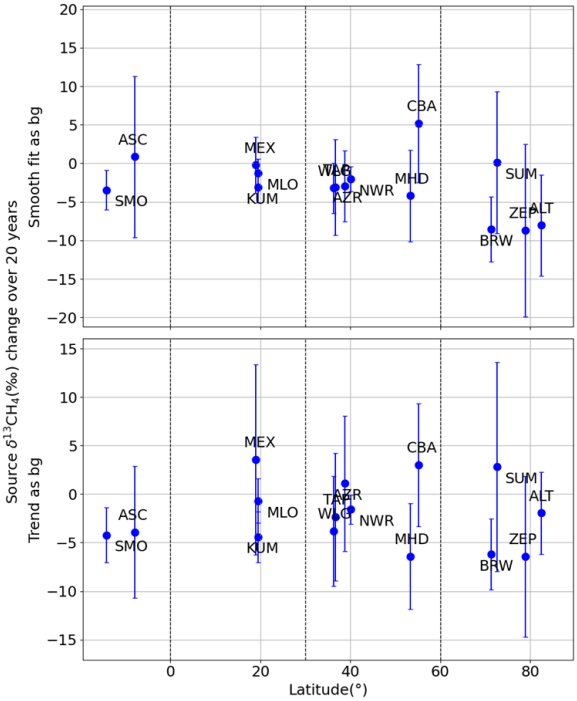

Figure 29: Source $\delta^{13}CH_4$ change in 20-year

As for the multi-year changes in the source $\delta^{13}CH_4$, we suggest that this reflects the strengthening of the more depleted emission component in the mixed $\delta^{13}CH_4$ we obtained.

For the more regional and short-term change components obtained by using smooth fit as background, they are less affected by OH. Therefore, we suggest that the downward trend of this isotope signal in the high-latitude region shows the strengthening of the microbial component in the mixed isotope signal on the regional scale.

Fig. 29 summarizes the changes in the source $\delta^{13}CH_4$ of each station over 20 years, which is obtained by multiplying the slope from Fig. 23 on 20-year. In terms of regional source $\delta^{13}CH_4$, the high-latitude stations in the Northern Hemisphere have a decrease of about 8‰ in 20 years. For mid- and low-latitude stations, the change is less than 5‰.

This can also be explained by the latitudinal gradients we discussed in section 4.3, which is related to the spatial distribution of different emissions and their $\delta^{13}CH_4$. Therefore, assuming that the emissions of microbial in northern mid and low-latitudes have also increased, the depletion effect on the mixed signal will not be as obvious as in northern high-latitude areas.

4.5 Explanation of differences between model and observation

In this study, we also used the output data of the inversion model. Although the model can better reproduce the long-term variation trend of the $\delta^{13}CH_4$ observation series with the addition of $\delta^{13}CH_4$

data than using CH_4 data alone for assimilationBasu et al. [2022], we found that it still cannot well represent the seasonal cycle of $\delta^{13}CH_4$.

By observing the original time series (Fig. 24) and the smooth seasonal cycle, we found that the model underestimated the seasonal cycle of each station. This is similar to the result of Kangasaho et al. [2022].

By applying the Miller & tans method to the model, we analyzed the mean seasonality of its source $\delta^{13}CH_4$ and compared it with the results obtained using observational data (Fig. 28). The results show that for the northern high latitudes, although the model can effectively reproduce its minimum values, for other times, the model overestimates the values of source $\delta^{13}CH_4$, which indicates that there is still a possibility of underestimation of the emission intensity and duration of high-latitude microbial.

For the northern mid and low-latitude regions, the model seems to overestimate both the level and seasonality of $\delta^{13}CH_4$, which indicates the possible presence of more enriched signals in these regions.

Considering the resolution of the model, its representation of the shortest-term regional variables may not be good enough compared with observations, which may also be a possible reason for the difference, which is reflected in the underestimation of regional wetland emissions in northern high latitudes and fossil emissions in mid- and low-latitude.

4.6 Future Improvements

In this study, we have conducted multiple analyses of the time series of CH_4 and $\delta^{13}CH_4$ to explore their seasonal characteristics and inter-annual variations. We found that, for $\delta^{13}CH_4$, seasonal decomposition seems difficult to study its seasonal inter-annual variations, so we used the Miller & Tans method to separate it from the background. However, this is accompanied by large uncertainties, which largely depend on how well we fit the original data, and for southern hemisphere sites, this brings large errors. Therefore, independent measurements may be more effective as a background method (Ballantyne et al. [2010], Umezawa et al. [2012]).

The difference between models and observations shows that the current understanding of the spatial distribution of emissions and their $\delta^{13}CH_4$ is not perfect, and more $\delta^{13}CH_4$ observations are needed, especially in tropical and high-emission regions, such as China and India.

Also, $\delta D - CH_4$ is another important information that may help to better constrain the source and sink, more and longer measurements are needed in future.

5 Conclusions

In the first part of this project, we measured surface flask samples of two IMAU methane isotope measurement project in the IMAU Stable isotope lab and compared them with NOAA/INSTAAR measurements and long-term time series. The results show that after quality control and offset correction, our $\delta^{13}CH_4$ measurements can well reproduce the INSTAAR results and show consistent seasonality with the long-term series. Although there is a lack of long-term time series for ISAMO samples, they still show obvious seasonal characteristics in single year and are consistent with the long-term series of stations at similar latitudes. Similarly, for $\delta D - CH_4$ measurements, there is a lack of long-term comparative data, but after linking, its latitudinal gradient and seasonal characteristics are still consistent with NOAA's past measurements.

In the second part, we analyzed the long-term time series of CH_4 and $\delta^{13}CH_4$ measured by NOAA on surface flask samples at 18 stations. We found that:

CH_4 and $\delta^{13}CH_4$ show clear average seasonality and similar characteristics in their individual hemispheres. In the southern hemisphere, CH_4 has a minimum in March and a maximum in September, while $\delta^{13}CH_4$ shows opposite seasonal characteristics. In the Northern Hemisphere, CH_4 reaches its minimum in July, and the seasonal characteristics of $\delta^{13}CH_4$ are more affected by seasonal emissions rather than the OH sink and do not show the opposite variation characteristics corresponding to CH_4.

The seasonal amplitude of CH_4 in northern high latitudes shows a different inter-annual variation trend from other regions, which may be caused by the enhancement of high-latitude wetland emissions. However, we did not find a significant inter-annual trend in the seasonality of $\delta^{13}CH_4$. After further using the Miller & Tans method, we use smooth fit and trend as two different backgrounds and obtain the corresponding source $\delta^{13}CH_4$. We found that in the Northern Hemisphere, the regional source $\delta^{13}CH_4$ contains obvious seasonality, and this seasonality is still exist at a larger temporal and spatial scale.

Combined with model emission data, the seasonality of $\delta^{13}CH_4$ in the Northern Hemisphere is mainly dominated by regional emissions, especially microbial sources.

There is a latitudinal gradient in the seasonal cycle amplitude and source $\delta^{13}CH_4$, which is related to the spatial distribution of emissions and their $\delta^{13}CH_4$. This is reflected in the relatively high proportion of fossils with weaker seasonality in low and middle latitudes than high latitudes. At the same time, the $\delta^{13}CH_4$ value of the source is enriched from high latitudes to the equator, which together leads to a decrease in the seasonal amplitude of CH_4 and $\delta^{13}CH_4$ from the arctic to the equator.

After analyzing the inter-annual trend of source $\delta^{13}CH_4$, we found that at high-latitude stations in the Northern Hemisphere, the regional source $\delta^{13}CH_4$ showed a downward trend, with a depletion of about 10‰ in the past 20 years, while at mid- and low-latitudes, with a smaller difference of 5‰ or less. This further proves the strengthening of depleted isotope signals in high-latitude regions of the Northern Hemisphere, that is, the strengthening of microbial emissions. For mid- and low-latitudes, due to the higher proportion of fossils compared to high latitudes and the relatively enriched $\delta^{13}CH_4$ values in emissions (still more depleted than the background value), the source $\delta^{13}CH_4$ also show a downward trend, but it is not obvious.

The difference between the Inverse model and observations indicates that due to the possible lack of regional processes, there are still deficiencies in the representation of high-latitude microbial emissions, while for mid- and low-latitude regions, fossil fuel emissions may be underestimated. The imperfect expression of sinks could be another reason, which requires further investigation of $\delta^{13}CH_4$ and $\delta D - CH_4$ observations in more regions.

Acknowledgement

I would like to express my deepest gratitude to my primary supervisor, Prof. Dr. Thomas Röckmann, thank you for your invaluable insights, suggestions, and support throughout this project.

Special thanks go to my daily supervisor, Dr. Bibhasvata Dasgupta, thank you for your engaging in discussions and for patiently answering my questions during the project.

I am also immensely grateful to other members of the IMAU APCG team. Carina, Chloe, Jacoline, and Chih-Chang, thank you for your patient guidance and assistance during the lab work. Additionally, I would like to extend my thanks to the NOAA team and the ISAMO team for providing valuable samples, data and suggestions, as well as to Sourish Basu for the model output. Without your support, this project would not have been possible.

Moreover, I wish to thank my friends, Rens, Ruoke, Raky, Baihui, Weihan and Xiaoheng, for their support throughout my master's studies and daily life. I am also deeply thankful to my family for their unwavering support. Finally, I would like to express my appreciation to my fellow students for making my master's experience unforgettable.

References

A. P. Ballantyne, J. B. Miller, and P. P. Tans. Apparent seasonal cycle in isotopic discrimination of carbon in the atmosphere and biosphere due to vapor pressure deficit. *Global Biogeochemical Cycles*, 24(3), 2010. doi: https://doi.org/10.1029/2009GB003623. URL https://agupubs.onlinelibrary.wiley.com/doi/abs/10.1029/2009GB003623.

J. M. Barlow, P. I. Palmer, and L. M. Bruhwiler. Increasing boreal wetland emissions inferred from reductions in atmospheric ch_4 seasonal cycle. *Atmospheric Chemistry and Physics Discussions*, 2016:1–38, 2016. doi: 10.5194/acp-2016-752. URL https://acp.copernicus.org/preprints/acp-2016-752/.

S. Basu, X. Lan, E. Dlugokencky, S. Michel, S. Schwietzke, J. B. Miller, L. Bruhwiler, Y. Oh, P. P. Tans, F. Apadula, L. V. Gatti, A. Jordan, J. Necki, M. Sasakawa, S. Morimoto, T. Di Iorio, H. Lee, J. Arduini, and G. Manca. Estimating emissions of methane consistent with atmospheric measurements of methane and δ^{13}c of methane. *Atmospheric Chemistry and Physics*, 22(23):15351–15377, 2022. doi: 10.5194/acp-22-15351-2022. URL https://acp.copernicus.org/articles/22/15351/2022/.

M. Brass and T. Röckmann. Continuous-flow isotope ratio mass spectrometry method for carbon and hydrogen isotope measurements on atmospheric methane. *Atmospheric measurement techniques*, 3(6):1707–1721, 12 2010. doi: 10.5194/amt-3-1707-2010. URL https://doi.org/10.5194/amt-3-1707-2010.

J.G. Canadell, P.M.S. Monteiro, M.H. Costa, L. Cotrim da Cunha, P.M. Cox, A.V. Eliseev, S. Henson, M. Ishii, S. Jaccard, C. Koven, A. Lohila, P.K. Patra, S. Piao, J. Rogelj, S. Syampungani, S. Zaehle, and K. Zickfeld. *Global Carbon and other Biogeochemical Cycles and Feedbacks*, page 673–816. Cambridge University Press, Cambridge, United Kingdom and New York, NY, USA, 2021. doi: 10.1017/9781009157896.007.

E. Dowd, C. Wilson, M. P. Chipperfield, E. Gloor, A. Manning, and R. Doherty. Decreasing seasonal cycle amplitude of methane in the northern high latitudes being driven by lower-latitude changes in emissions and transport. *Atmospheric Chemistry and Physics*, 23(13):7363–7382, 2023. doi: 10.5194/acp-23-7363-2023. URL https://acp.copernicus.org/articles/23/7363/2023/.

James D. East, Daniel J. Jacob, Nicholas Balasus, A. Anthony Bloom, Lori Bruhwiler, Zichong Chen, Jed O. Kaplan, Loretta J. Mickley, Todd A. Mooring, Elise Penn, Benjamin Poulter, Melissa P. Sulprizio, John R. Worden, Robert M. Yantosca, and Zhen Zhang. Interpreting the seasonality of atmospheric methane. *Geophysical Research Letters*, 51(10):e2024GL108494, 2024. doi: https://doi.org/10.1029/2024GL108494. URL https://agupubs.onlinelibrary.wiley.com/doi/abs/10.1029/2024GL108494. e2024GL108494 2024GL108494.

D. H. EHHALT. The atmospheric cycle of methane. *Tellus*, 26(1-2):58–70, 1974. doi: https://doi.org/10.1111/j.2153-3490.1974.tb01952.x. URL https://onlinelibrary.wiley.com/doi/abs/10.1111/j.2153-3490.1974.tb01952.x.

P. Forster, T. Storelvmo, K. Armour, W. Collins, J.-L. Dufresne, D. Frame, D.J. Lunt, T. Mauritsen, M.D. Palmer, M. Watanabe, M. Wild, and H. Zhang. *The Earth's Energy Budget, Climate Feedbacks, and Climate Sensitivity*, page 923–1054. Cambridge University Press, Cambridge, United Kingdom and New York, NY, USA, 2021. doi: 10.1017/9781009157896.009.

A. L. Ganesan, A. C. Stell, N. Gedney, E. Comyn-Platt, G. Hayman, M. Rigby, B. Poulter, and E. R. C. Hornibrook. Spatially resolved isotopic source signatures of wetland methane emissions. *Geophysical Research Letters*, 45(8):3737–3745, 2018. doi: https://doi.org/10.1002/2018GL077536. URL https://agupubs.onlinelibrary.wiley.com/doi/abs/10.1002/2018GL077536.

Vilma Kangasaho, Aki Tsuruta, Leif Backman, Pyry Mäkinen, Sander Houweling, Arjo Segers, Maarten Krol, Edward J. Dlugokencky, Sylvia Michel, James W. C. White, and Tuula Aalto. The role of emission sources and atmospheric sink in the seasonal cycle of ch4 and δ13-ch4: Analysis based on the atmospheric chemistry transport model tm5. *Atmosphere*, 13(6), 2022. ISSN 2073-4433. doi: 10.3390/atmos13060888. URL https://www.mdpi.com/2073-4433/13/6/888.

Charles D Keeling. The concentration and isotopic abundances of atmospheric carbon dioxide in

rural areas. *Geochimica et Cosmochimica Acta*, 13(4):322–334, 1958. ISSN 0016-7037. doi: https://doi.org/10.1016/0016-7037(58)90033-4. URL https://www.sciencedirect.com/science/article/pii/0016703758900334.

X. Lan, S. Basu, S. Schwietzke, L. M. P. Bruhwiler, E. J. Dlugokencky, S. E. Michel, O. A. Sherwood, P. P. Tans, K. Thoning, G. Etiope, Q. Zhuang, L. Liu, Y. Oh, J. B. Miller, G. Pétron, B. H. Vaughn, and M. Crippa. Improved constraints on global methane emissions and sinks using δ13c-ch4. *Global Biogeochemical Cycles*, 35(6):e2021GB007000, 2021. doi: https://doi.org/10.1029/2021GB007000. URL https://agupubs.onlinelibrary.wiley.com/doi/abs/10.1029/2021GB007000. e2021GB007000 2021GB007000.

X. Lan, J.W. Mund, A.M. Crotwell, M.J. Crotwell, E. Moglia, M. Madronich, D. Neff, and K.W. Thoning. Atmospheric methane dry air mole fractions from the noaa gml carbon cycle cooperative global air sampling network, 1983-2022. https://doi.org/10.15138/VNCZ-M766, 2023. Version: 2023-08-28.

S.E. Michel, J.R. Clark, B.H. Vaughn, M. Crotwell, M. Madronich, E. Moglia, D. Neff, and J. Mund. Stable isotopic composition of atmospheric methane (^{13}c) from the noaa gml carbon cycle cooperative global air sampling network, 1998-2022, 2023. URL https://doi.org/10.15138/9p89-1x02. Version: 2023-09-21.

John B. Miller and Pieter P. Tans. Calculating isotopic fractionation from atmospheric measurements at various scales. *Tellus. Series B, Chemical and physical meteorology*, 55(2):207–214, 4 2003. doi: 10.1034/j.1600-0889.2003.00020.x. URL https://doi.org/10.1034/j.1600-0889.2003.00020.x.

Shinji Morimoto, Shuji Aoki, Takakiyo Nakazawa, and Takashi Yamanouchi. Temporal variations of the carbon isotopic ratio of atmospheric methane observed at ny Ålesund, svalbard from 1996 to 2004. *Geophysical Research Letters*, 33(1), 2006. doi: https://doi.org/10.1029/2005GL024648. URL https://agupubs.onlinelibrary.wiley.com/doi/abs/10.1029/2005GL024648.

Euan G. Nisbet, Martin R. Manning, Ed J. Dlugokencky, Sylvia Englund Michel, Xin Lan, Thomas Röckmann, Hugo A. C. Denier van der Gon, Jochen Schmitt, Paul I. Palmer, Michael N. Dyonisius, Youmi Oh, Rebecca E. Fisher, David Lowry, James L. France, James W. C. White, Gordon Brailsford, and Tony Bromley. Atmospheric methane: Comparison between methane's record in 2006–2022 and during glacial terminations. *Global Biogeochemical Cycles*, 37(8):e2023GB007875, 2023. doi: https://doi.org/10.1029/2023GB007875. URL https://agupubs.onlinelibrary.wiley.com/doi/abs/10.1029/2023GB007875. e2023GB007875 2023GB007875.

Youmi Oh, Qianlai Zhuang, Lisa R. Welp, Licheng Liu, Xin Lan, Sourish Basu, Edward J. Dlugokencky, Lori Bruhwiler, John B. Miller, Sylvia E. Michel, Stefan Schwietzke, Pieter Tans, Philippe Ciais, and Jeffrey P. Chanton. Improved global wetland carbon isotopic signatures support post-2006 microbial methane emission increase. *Communications earth & environment*, 3(1), 7 2022. doi: 10.1038/s43247-022-00488-5. URL https://doi.org/10.1038/s43247-022-00488-5.

Peter J. Rousseeuw and Christophe Croux. Alternatives to the median absolute deviation. *Journal of the American Statistical Association*, 88(424):1273–1283, 1993. doi: 10.1080/01621459.1993.10476408. URL https://www.tandfonline.com/doi/abs/10.1080/01621459.1993.10476408.

Gerd Saueressig, John N. Crowley, Peter Bergamaschi, Christoph Brühl, Carl A. M. Brenninkmeijer, and Horst Fischer. Carbon 13 and d kinetic isotope effects in the reactions of ch4 with o(1 d) and oh: New laboratory measurements and their implications for the isotopic composition of stratospheric methane. *Journal of Geophysical Research: Atmospheres*, 106(D19):23127–23138, 2001. doi: https://doi.org/10.1029/2000JD000120. URL https://agupubs.onlinelibrary.wiley.com/doi/abs/10.1029/2000JD000120.

O. A. Sherwood, S. Schwietzke, V. A. Arling, and G. Etiope. Global inventory of gas geochemistry data from fossil fuel, microbial and burning sources, version 2017. *Earth System Science Data*, 9(2):639–656, 2017. doi: 10.5194/essd-9-639-2017. URL https://essd.copernicus.org/articles/9/639/2017/.

C. M. Spivakovsky, J. A. Logan, S. A. Montzka, Y. J. Balkanski, M. Foreman-Fowler, D. B. A. Jones, L. W. Horowitz, A. C. Fusco, C. A. M. Brenninkmeijer, M. J. Prather, S. C. Wofsy, and

M. B. McElroy. Three-dimensional climatological distribution of tropospheric oh: Update and evaluation. *Journal of Geophysical Research: Atmospheres*, 105(D7):8931–8980, 2000. doi: https://doi.org/10.1029/1999JD901006. URL https://agupubs.onlinelibrary.wiley.com/doi/abs/10.1029/1999JD901006.

Pieter P. Tans. On calculating the transfer of carbon-13 in reservoir models of the carbon cycle. *Tellus. Series A, Dynamic meteorology and oceanography*, 32(5):464, 1 1980. doi: 10.3402/tellusa.v32i5.10601. URL https://doi.org/10.3402/tellusa.v32i5.10601.

Kirk W. Thoning, Pieter P. Tans, and Walter D. Komhyr. Atmospheric carbon dioxide at Mauna Loa Observatory: 2. Analysis of the NOAA GMCC data, 1974–1985. *Journal of geophysical research*, 94(D6):8549–8565, 6 1989. doi: 10.1029/jd094id06p08549. URL https://doi.org/10.1029/jd094id06p08549.

Stanley C. Tyler, Andrew L. Rice, and Henry O. Ajie. Stable isotope ratios in atmospheric ch4: Implications for seasonal sources and sinks. *Journal of Geophysical Research: Atmospheres*, 112 (D3), 2007. doi: https://doi.org/10.1029/2006JD007231. URL https://agupubs.onlinelibrary.wiley.com/doi/abs/10.1029/2006JD007231.

T. Umezawa, C. A. M. Brenninkmeijer, T. Röckmann, C. van der Veen, S. C. Tyler, R. Fujita, S. Morimoto, S. Aoki, T. Sowers, J. Schmitt, M. Bock, J. Beck, H. Fischer, S. E. Michel, B. H. Vaughn, J. B. Miller, J. W. C. White, G. Brailsford, H. Schaefer, P. Sperlich, W. A. Brand, M. Rothe, T. Blunier, D. Lowry, R. E. Fisher, E. G. Nisbet, A. L. Rice, P. Bergamaschi, C. Veidt, and I. Levin. Interlaboratory comparison of δ^{13}c and δd measurements of atmospheric ch_4 for combined use of data sets from different laboratories. *Atmospheric Measurement Techniques*, 11(2):1207–1231, 2018. doi: 10.5194/amt-11-1207-2018. URL https://amt.copernicus.org/articles/11/1207/2018/.

Taku Umezawa, Toshinobu Machida, Shuji Aoki, and Takakiyo Nakazawa. Contributions of natural and anthropogenic sources to atmospheric methane variations over western siberia estimated from its carbon and hydrogen isotopes. *Global Biogeochemical Cycles*, 26(4), 2012. doi: https://doi.org/10.1029/2011GB004232. URL https://agupubs.onlinelibrary.wiley.com/doi/abs/10.1029/2011GB004232.

J.W.C. White, B.H. Vaughn, and S.E. Michel. Stable isotopic composition of atmospheric methane (^{2}h) from the noaa esrl carbon cycle cooperative global air sampling network, 2005-2009. ftp://aftp.cmdl.noaa.gov/data/trace_gases/ch4h2/flask/, 2016. Version: 2016-04-26.

Ceres A. Woolley Maisch, Rebecca E. Fisher, James L. France, David Lowry, Mathias Lanoisellé, Thomas G. Bell, Grant Forster, Alistair J. Manning, Sylvia E. Michel, Alice E. Ramsden, Mingxi Yang, and Euan G. Nisbet. Methane source attribution in the uk using multi-year records of ch4 and δ13c. *Journal of Geophysical Research: Atmospheres*, 128(21):e2023JD039098, 2023. doi: https://doi.org/10.1029/2023JD039098. URL https://agupubs.onlinelibrary.wiley.com/doi/abs/10.1029/2023JD039098. e2023JD039098 2023JD039098.

Kunxiaojia Yuan, Fa Li, Gavin McNicol, Min Chen, Alison Hoyt, Sara Knox, William J. Riley, Robert Jackson, and Qing Zhu. Boreal–Arctic wetland methane emissions modulated by warming and vegetation activity. *Nature climate change*, 2 2024. doi: 10.1038/s41558-024-01933-3. URL https://doi.org/10.1038/s41558-024-01933-3.

A Appendix

Table 3: Sampling stations including ISAMO project, where 4 BUDS stations are sampled at the same places of NOAA sites

Station name	**Site code**	**Latitude**	**Longitude**
Alert, Nunavut Canada	ALT	82.4508	-62.5072
Ny-Alesund, Svalbard Norway and Sweden	ZEP	78.9067	11.8883
Summit, Greenland	SUM	72.5962	-38.422
Barrow Atmospheric Baseline Observatory , USA	BRW (Also for BUDS)	71.32	-156.6
Cold Bay, Alaska, USA	CBA	55.2	-162.72
Mace Head, Ireland	MHD	53.33	-9.9
Niwot Ridge, Colorado , USA	NWR	40.05	-105.58
Terceira Island, Azores Portugal	AZR	38.75	-27.08
Tae-ahn Peninsula, Republic of Korea	TAP	36.73	126.13
Mt. Waliguan Peoples Republic of China	WLG	36.27	100.92
Mauna Loa, Hawaii , USA	MLO (Also for BUDS)	19.53	-155.58
Cape Kumukahi, Hawaii, USA	KUM	19.52	-154.82
High Altitude Global Climate Observation Center, Mexico	MEX	18.9841	-97.311
Ascension Island, UK	ASC	-7.9667	-14.4
Tutuila, American Samoa	SMO (Also for BUDS)	-14.25	-170.57
Cape Grim, Tasmania, Australia	CGO (Also for BUDS)	-40.68	144.68
Baring Head Station, New Zealand	BHD	-41.4083	174.871
South Pole, Antarctica , USA	SPO	-89.98	-24.8
Izana, Tenerife, Canary Islands, Spain	ISAMO IZO	28.3	-16.5
Tenerife	ISAMO IEO	28.0	-16.0
Cape Verde	ISAMO CVAO	16.9	-24.9
Ragged Point, Barbados	ISAMO RPB	13.3	-59.9
Amazon Tall Tower Observatory	ISAMO ATTO	-2.0	-59.0

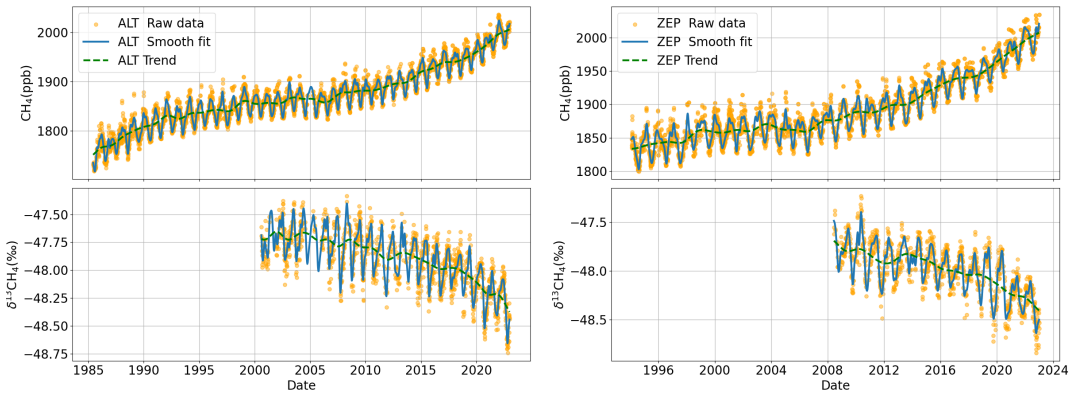

(a) ALT

(b) ZEP

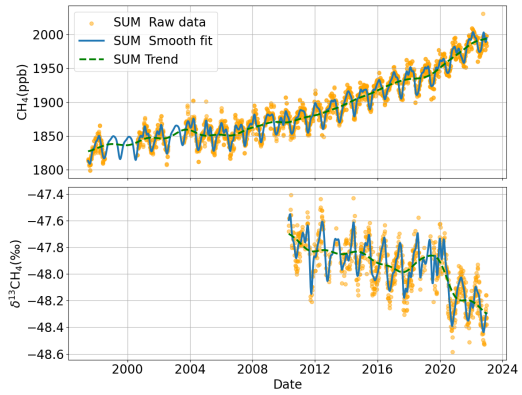

(c) SUM

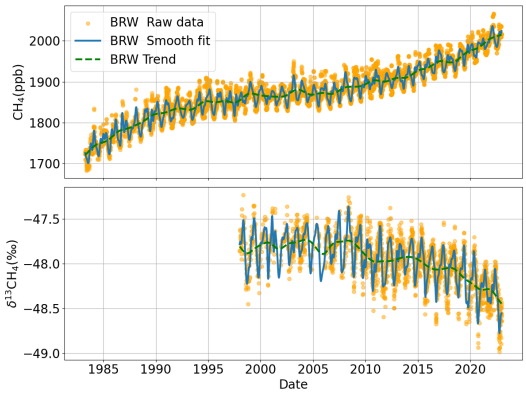

(d) BRW

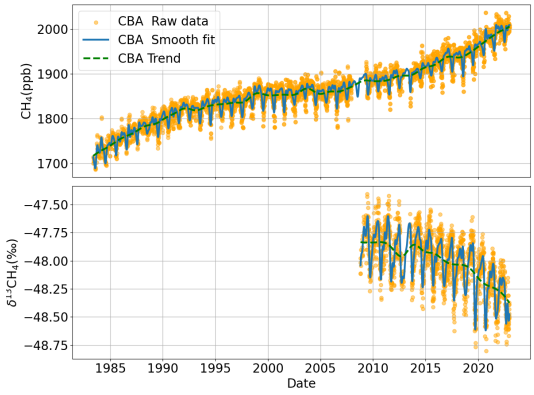

(e) CBA

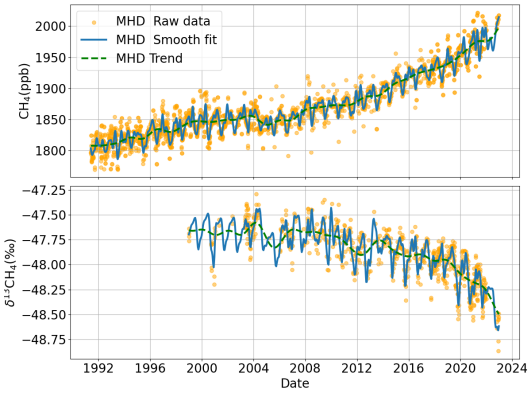

(f) MHD

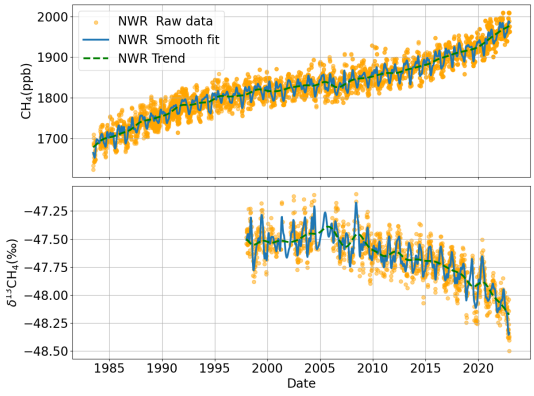

(g) NWR

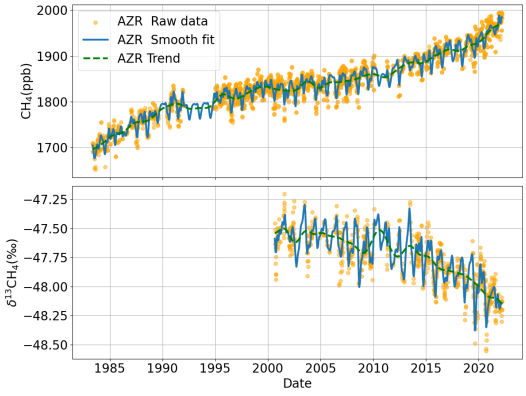

(h) AZR

Figure 1: CH_4 and $\delta^{13}CH_4$ time series Decomposition of 18 NOAA stations-part 1

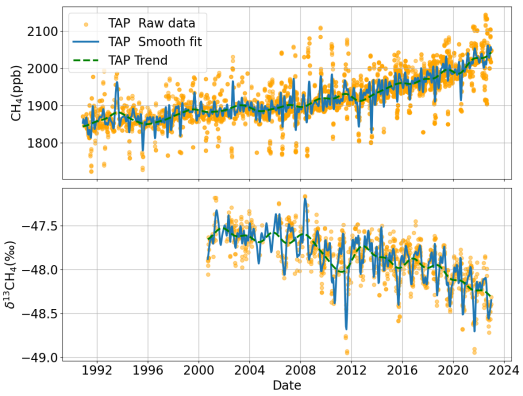

(a) TAP

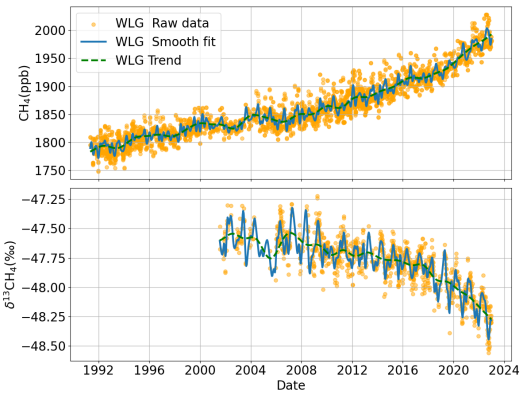

(b) WLG

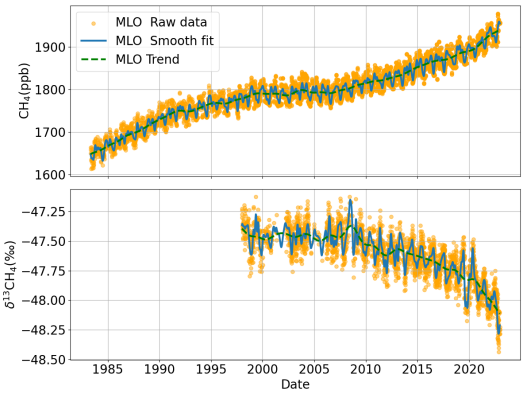

(c) MLO

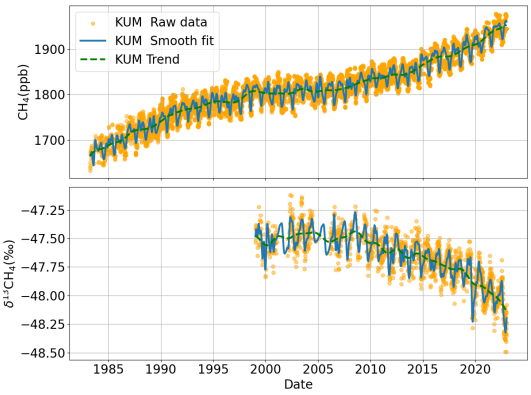

(d) KUM

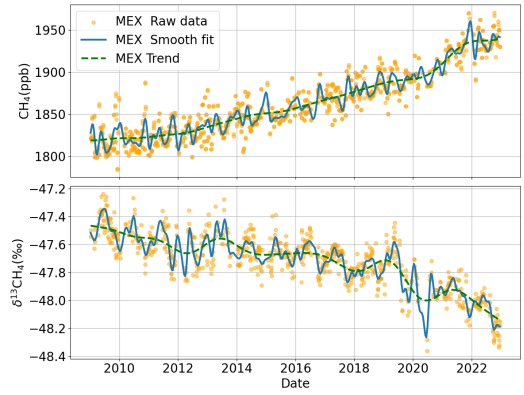

(e) MEX

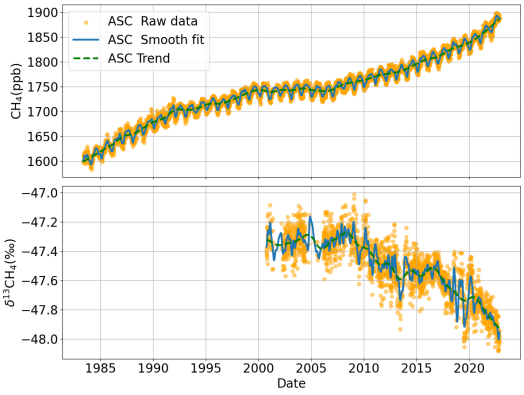

(f) ASC

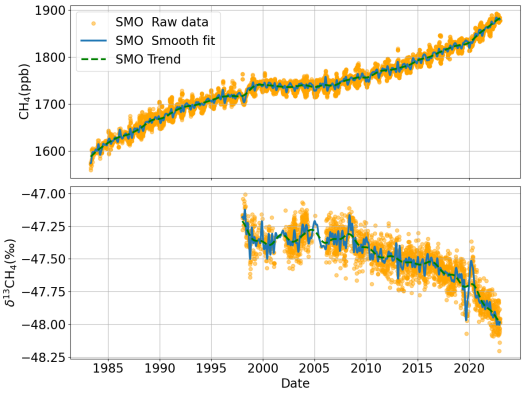

(g) SMO

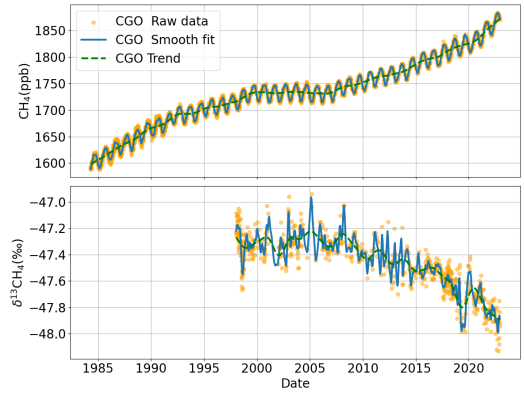

(h) CGO

Figure 2: CH_4 and $\delta^{13}CH_4$ time series Decomposition of 18 NOAA stations-part 2

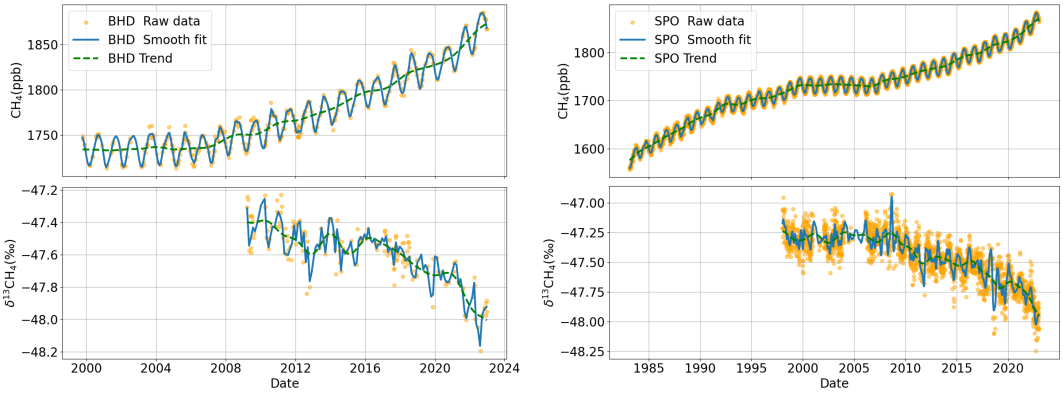

(a) BHD

(b) SPO

Figure 3: CH_4 and $\delta^{13}CH_4$ time series Decomposition of 18 NOAA stations-part 3

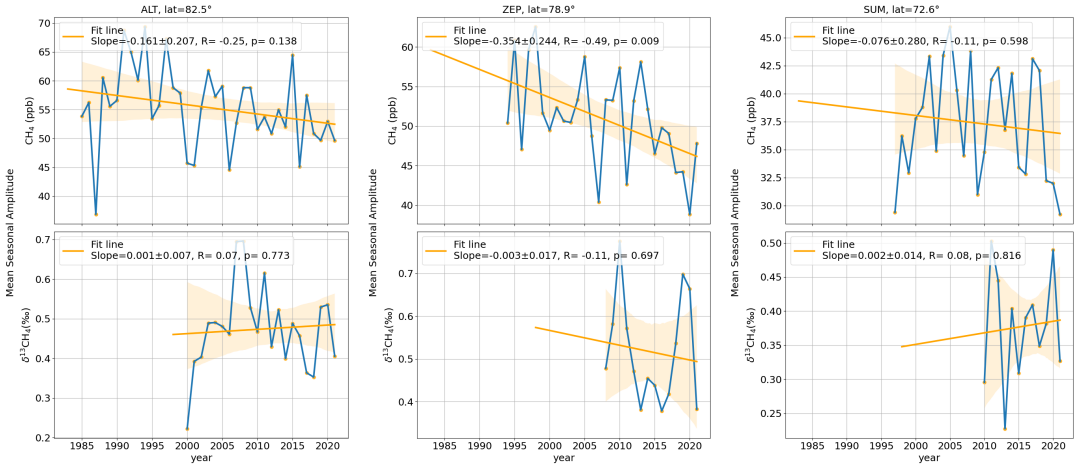

(a) ALT (b) ZEP (c) SUM

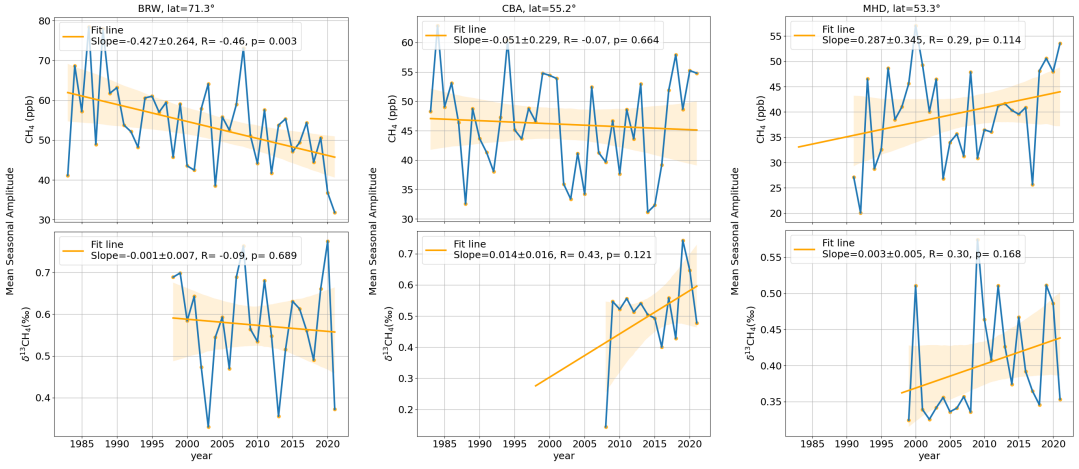

(d) BRW (e) CBA (f) MHD

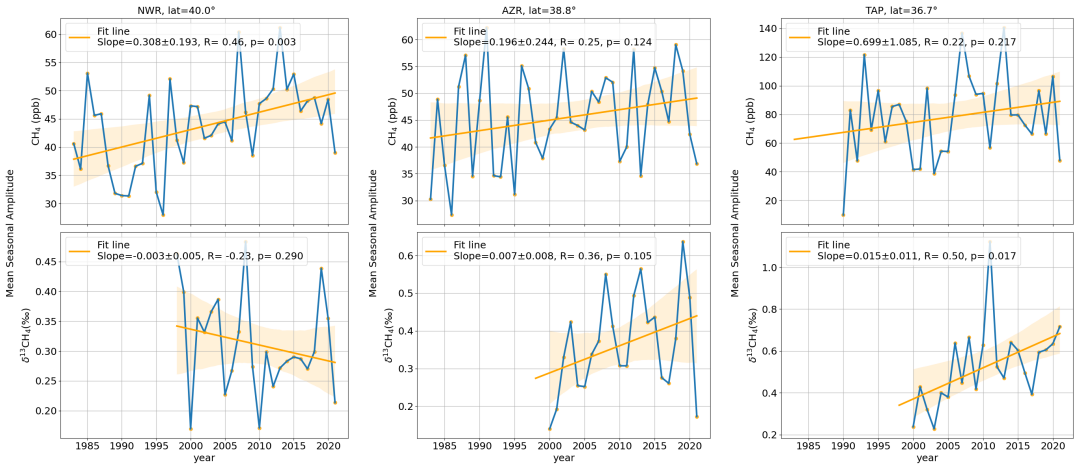

(g) NWR (h) AZR (i) TAP

Figure 4: Inter-annual trend of seasonal amplitude CH_4 (upper) and $\delta^{13}CH_4$ (lower)-part 1

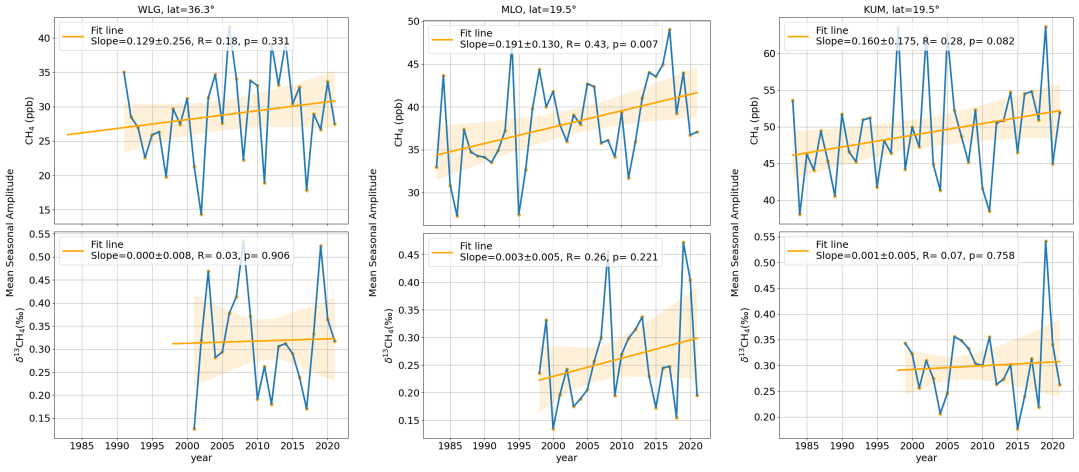

(a) WLG (b) MLO (c) KUM

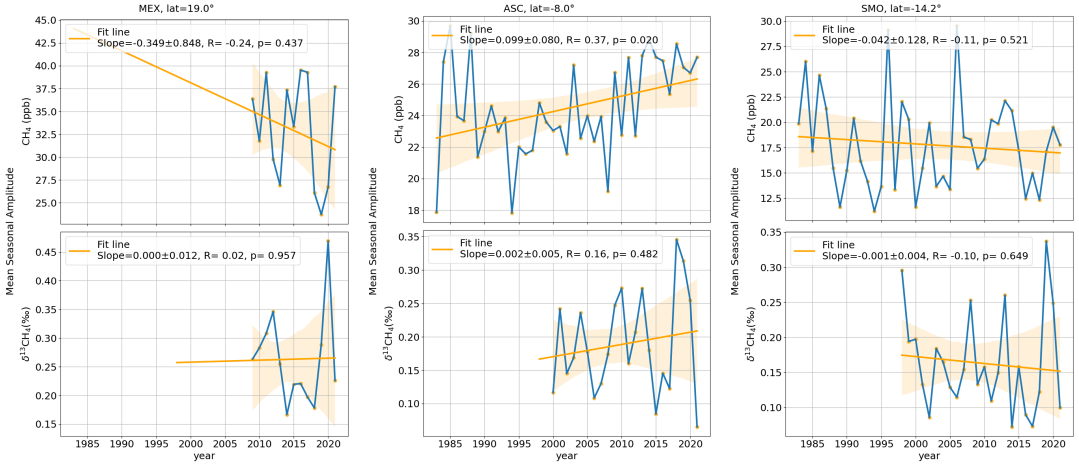

(d) MEX (e) ASC (f) SMO

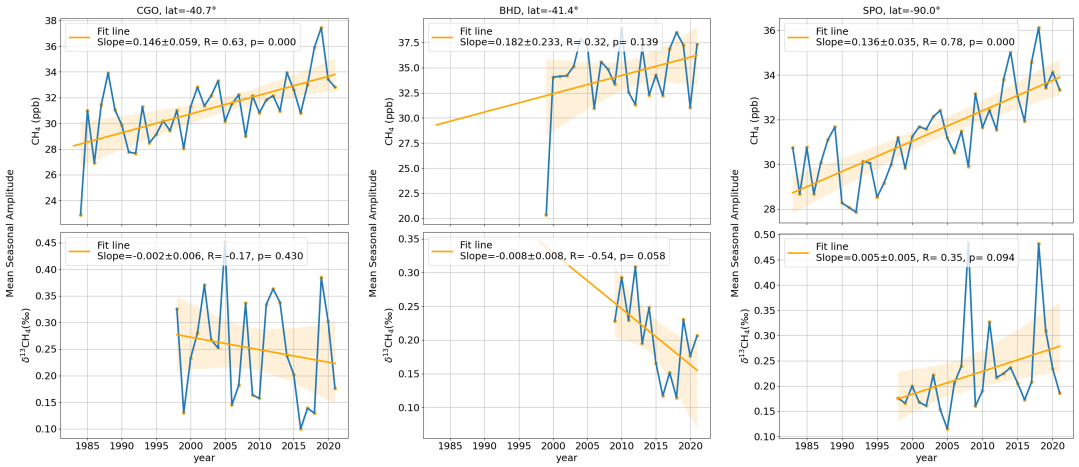

(g) CGO (h) BHD (i) SPO

Figure 5: Inter-annual trend of seasonal amplitude CH_4 (upper) and $\delta^{13}CH_4$ (lower)-part 2

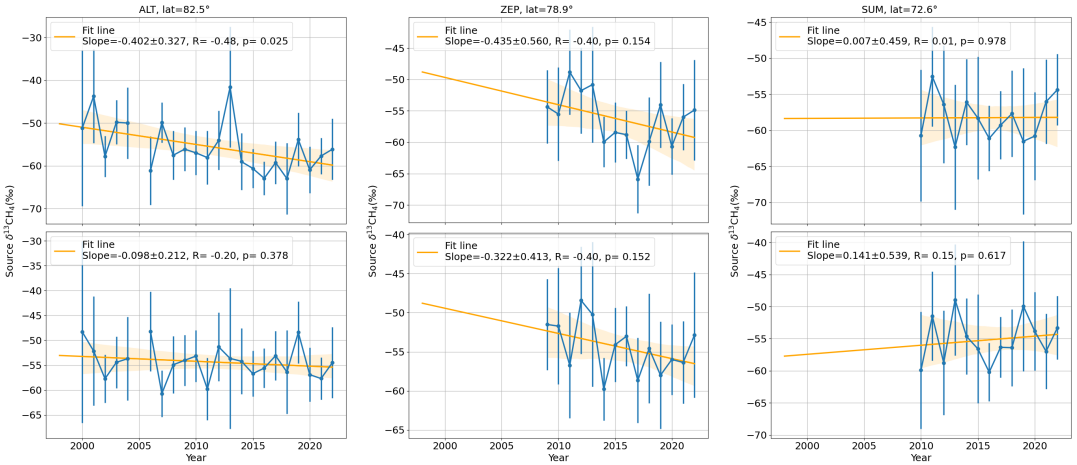

(a) ALT (b) ZEP (c) SUM

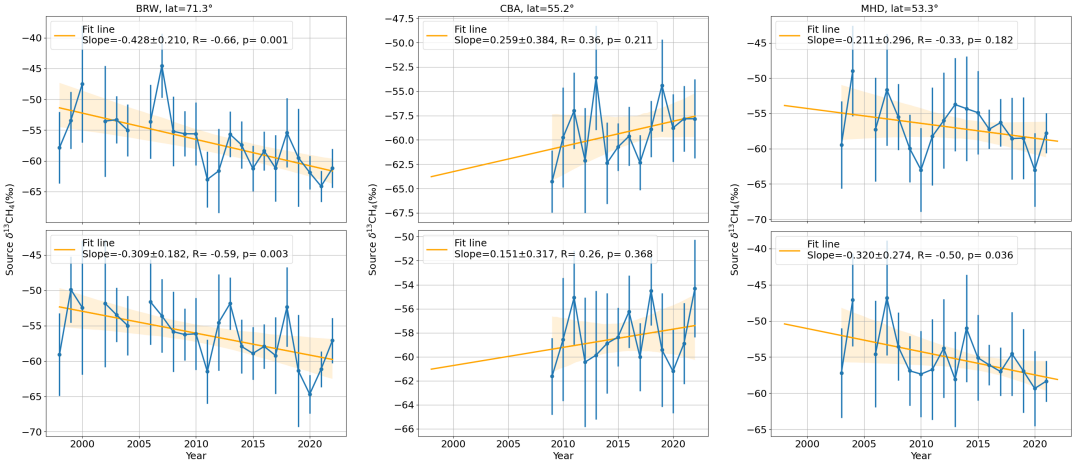

(d) BRW (e) CBA (f) MHD

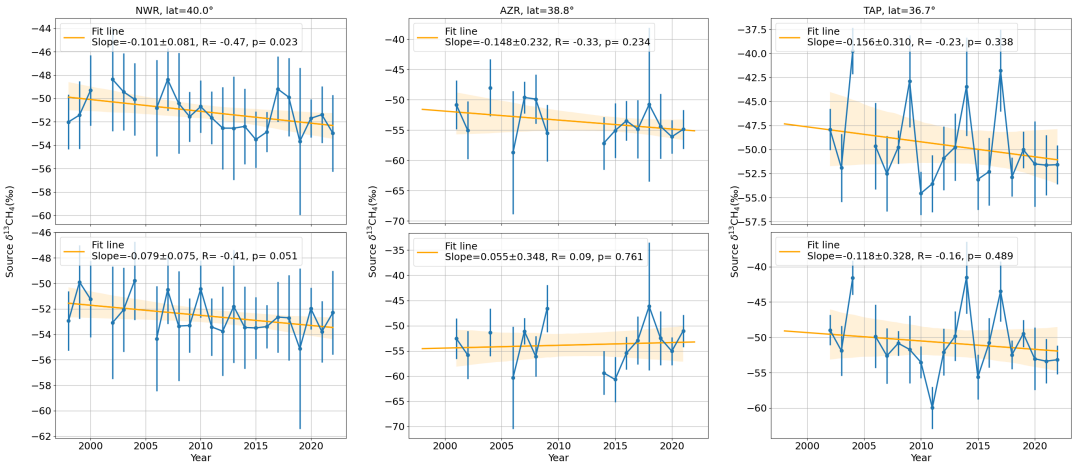

(g) NWR (h) AZR (i) TAP

Figure 6: Inter-annual trend of source $\delta^{13}CH_4$, BG1 (upper), BG2 (lower)-part 1

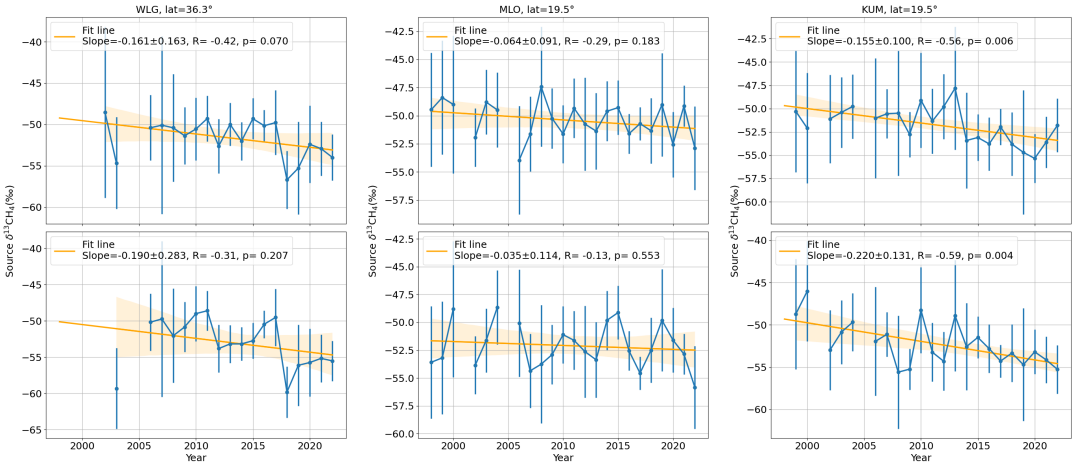

(a) WLG (b) MLO (c) KUM

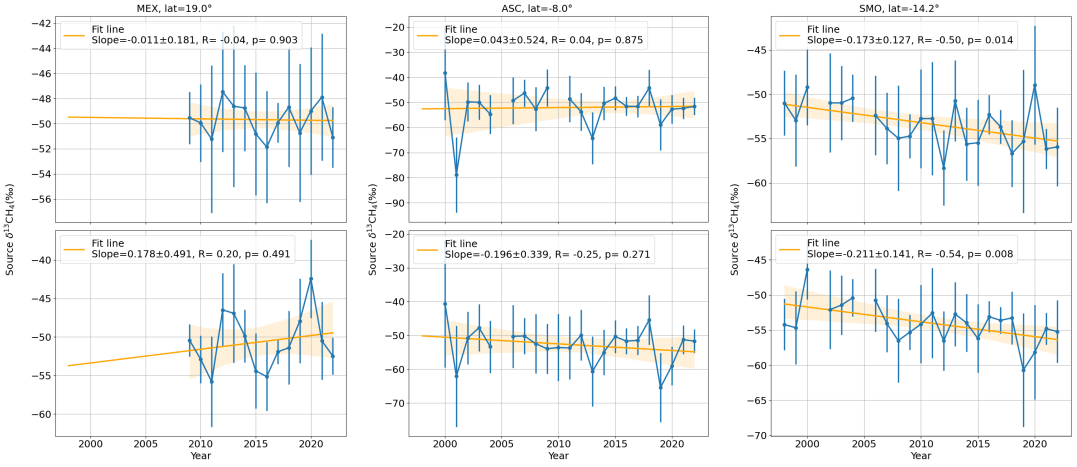

(d) MEX (e) ASC (f) SMO

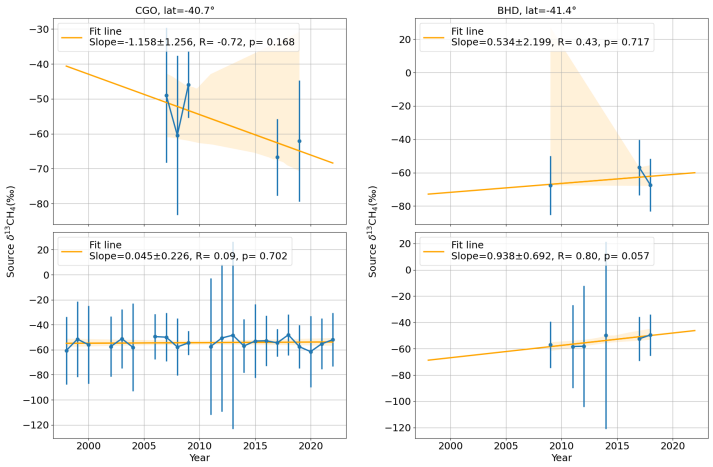

(g) CGO (h) BHD

Figure 7: Inter-annual trend of source $\delta^{13}CH_4$, BG1 (upper), BG2 (lower)-part 2

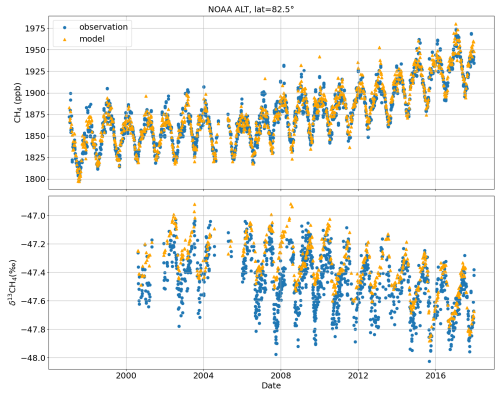

(a) ALT

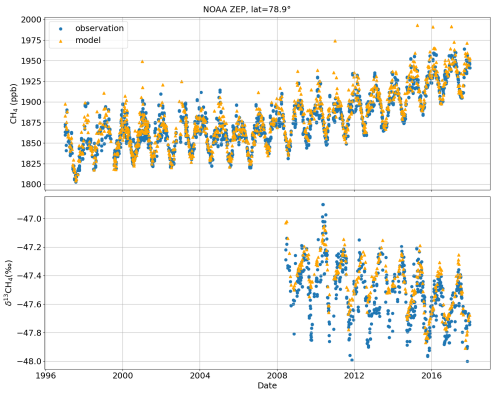

(b) ZEP

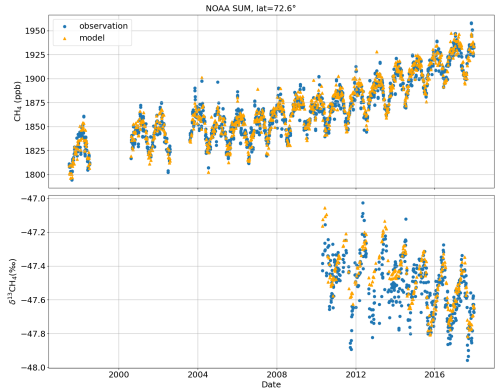

(c) SUM

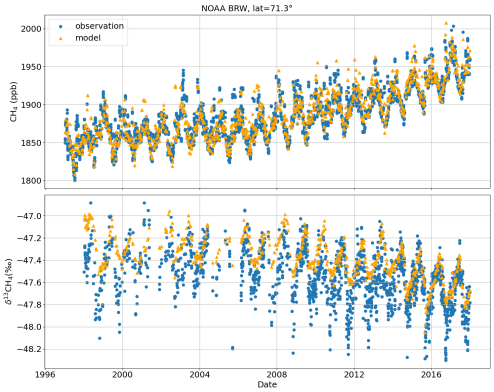

(d) BRW

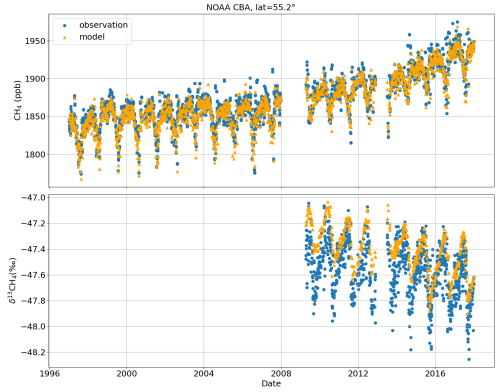

(e) CBA

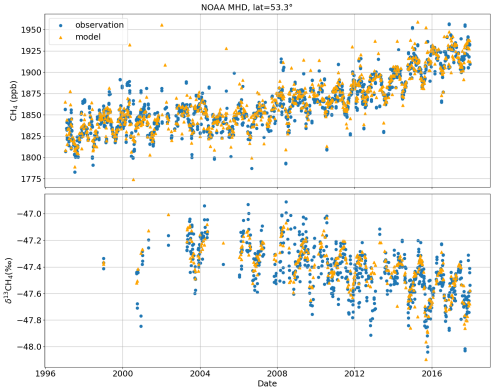

(f) MHD

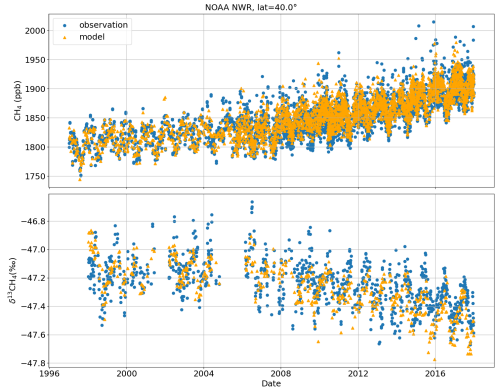

(g) NWR

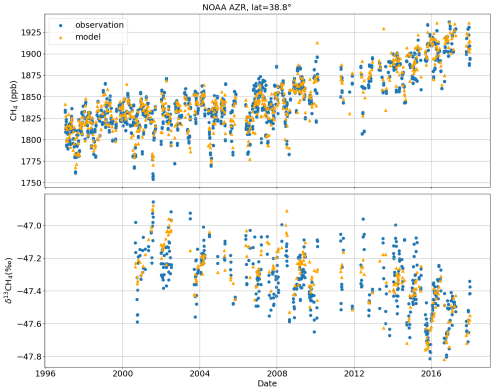

(h) AZR

Figure 8: CH_4 and $\delta^{13}CH_4$ timeseries, observation and model part 1

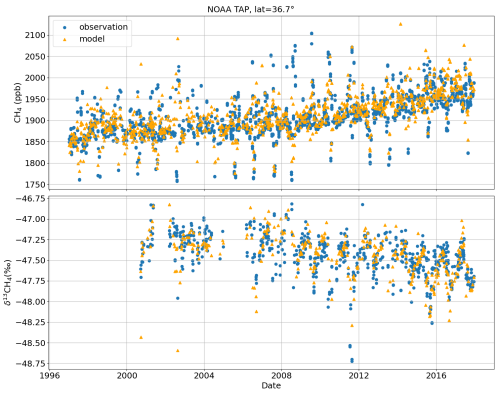

(a) TAP

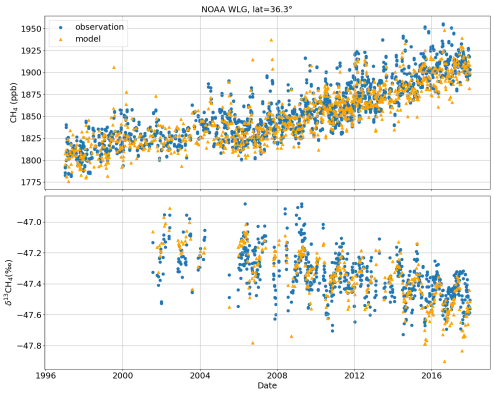

(b) WLG

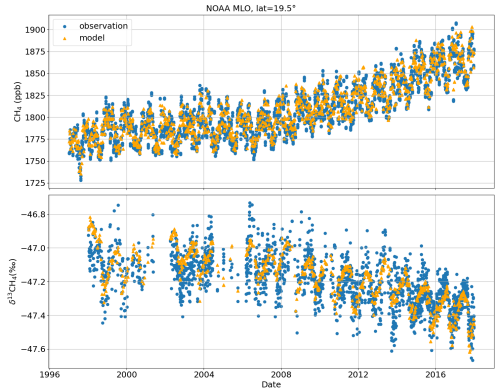

(c) MLO

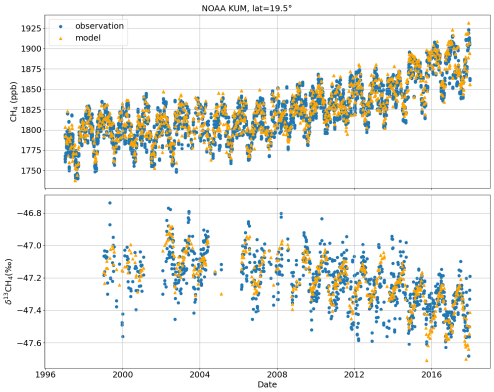

(d) KUM

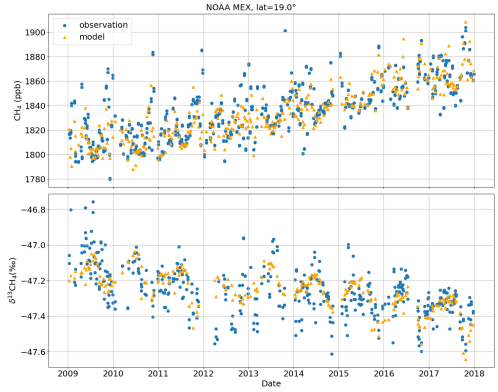

(e) MEX

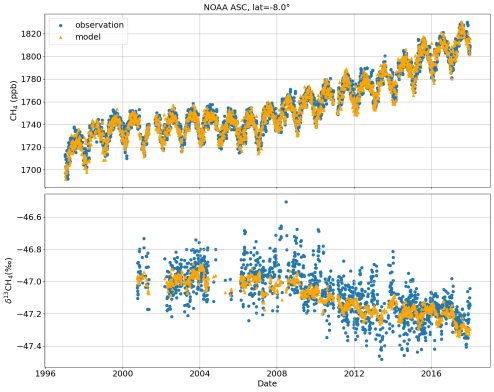

(f) ASC

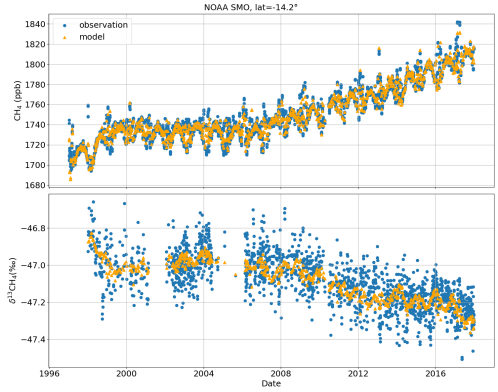

(g) SMO

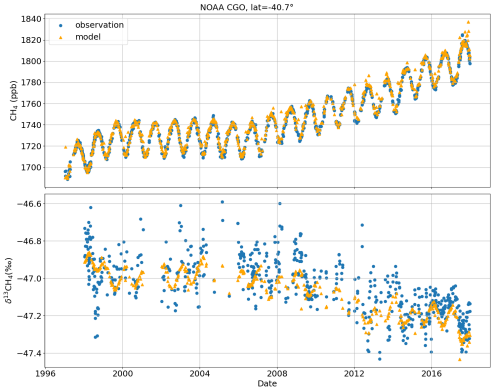

(h) CGO

Figure 9: CH_4 and $\delta^{13}CH_4$ timeseries, observation and model part 2

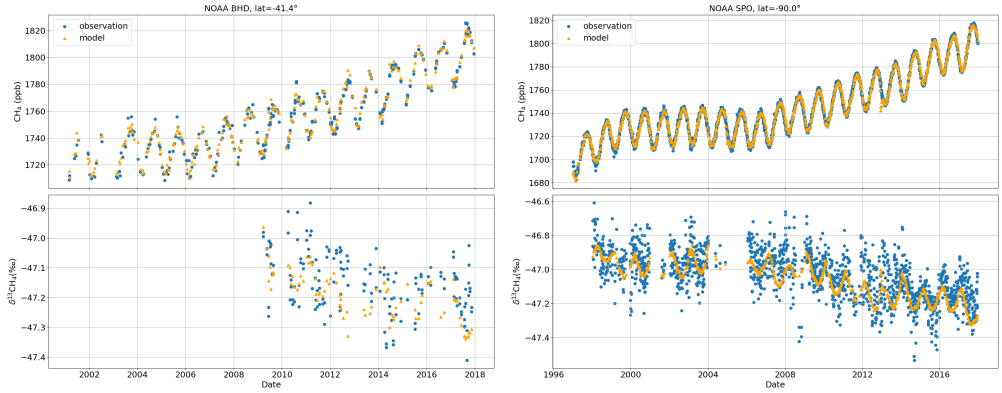

(a) BHD (b) SPO

Figure 10: CH_4 and $\delta^{13}CH_4$ timeseries, observation and model part 3

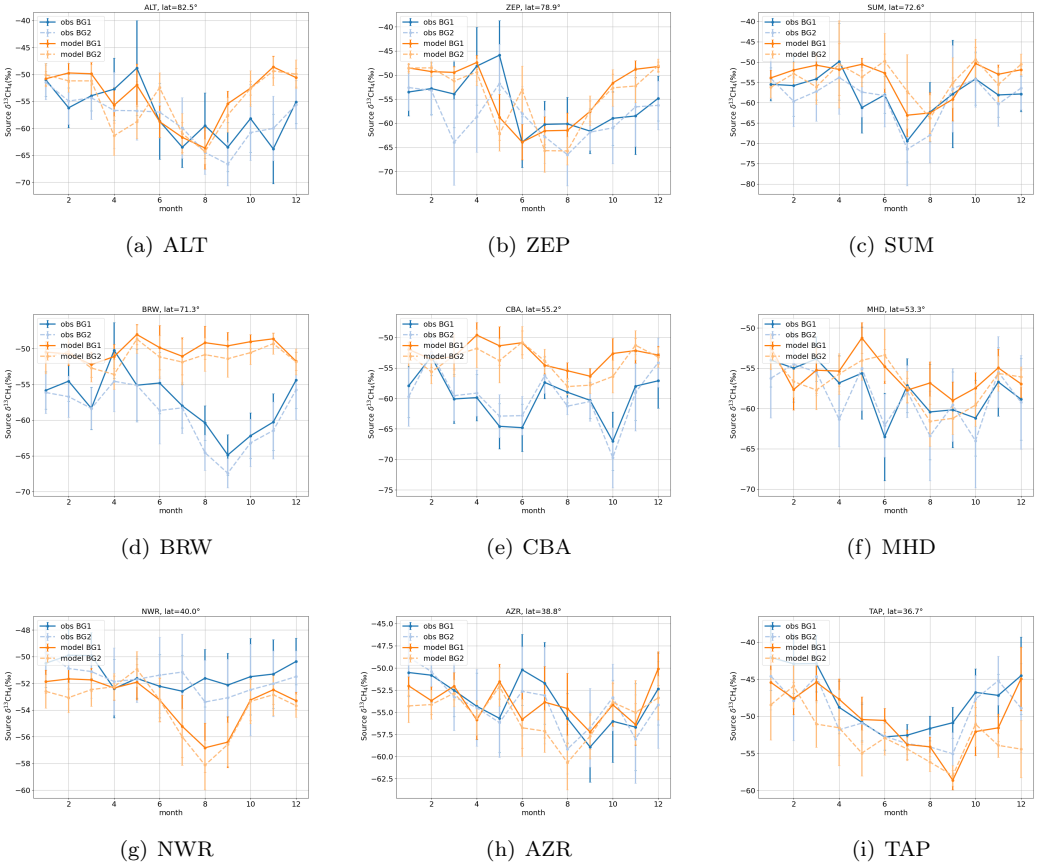

(a) ALT (b) ZEP (c) SUM

(d) BRW (e) CBA (f) MHD

(g) NWR (h) AZR (i) TAP

Figure 11: Mean seasonality of source $\delta^{13}CH_4$ in observation and model, BG1 (upper), BG2 (lower)- part 1

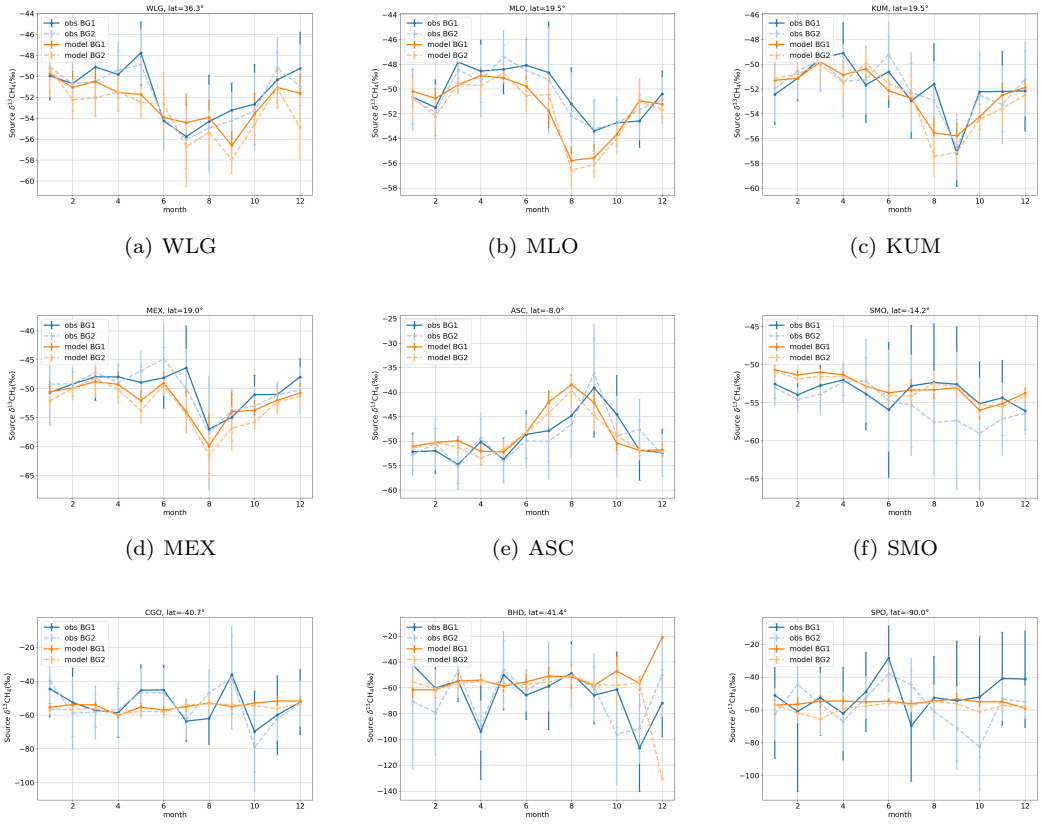

(a) WLG (b) MLO (c) KUM

(d) MEX (e) ASC (f) SMO

(g) CGO (h) BHD (i) SPO

Figure 12: Mean seasonality of source $\delta^{13}CH_4$ in observation and model, BG1 (upper), BG2 (lower)-part 2